

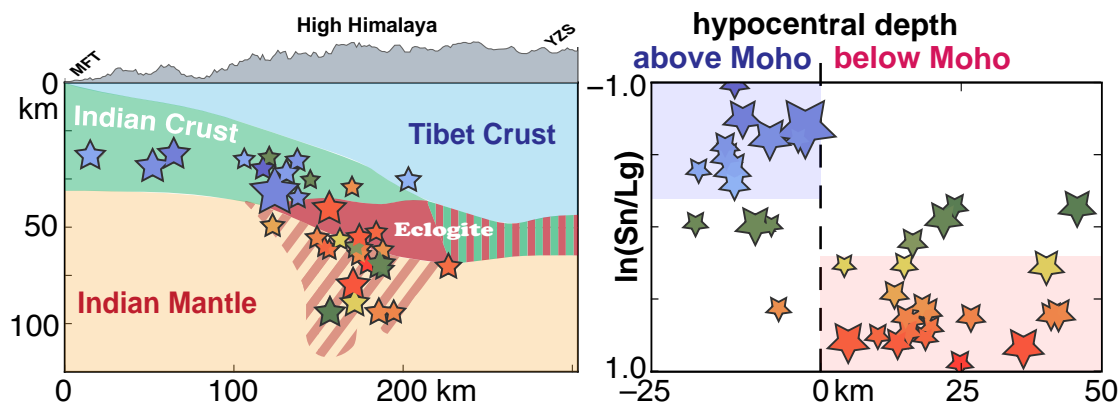
Numerous Tibetan lower-crustal and upper-mantle earthquakes detected by Sn/Lg ratios suggest crustal delamination or drip tectonics

Xiaohan Song, Simon L. Klemperer

Department of Geophysics, Stanford University, Stanford, CA 94305, USA

Highlights:

- Our single-station S_n/L_g method distinguishes above-Moho from below-Moho earthquakes
- In 20 years, two areas in Tibet/Himalaya have $>100 m_b \geq 3.5$ below-Moho earthquakes
- These two areas likely also have $>100 m_b \geq 3.5$ earthquakes between 30 km and the Moho
- Both the above- and below-Moho earthquakes could all be in crustal rocks (eclogite)
- We infer drip tectonics beneath the Himalaya, & delamination tectonics below NW Tibet



1
2
3
4
5
6
7 Numerous Tibetan lower-crustal and upper-mantle earthquakes
8 detected by Sn/Lg ratios suggest crustal delamination or drip
9 tectonics

10
11 Xiaohan Song, Simon L. Klemperer

12
13 *Department of Geophysics, Stanford University, Stanford, CA 94305, USA*
14
15

16
17 A B S T R A C T

18
19 Whether intermediate-depth earthquakes beneath Tibet and the Himalaya are in the lower crust or upper mantle
20 should provide insight into rheology, hence composition and temperature, of continental lower crust & upper
21 mantle. Based on the waveguide theory that earthquakes respectively above or below the Moho will excite higher
22 Lg energy or higher Sn energy, we develop an Sn/Lg amplitude-ratio analysis using a single permanent station
23 to investigate earthquake depths with respect to the Moho. First, we use synthetics to show the ubiquitous sharp
24 increase of the Sn/Lg ratio for hypocenters beneath the crust. A deep-crustal high- v_s layer appropriate for
25 eclogitized Indian lower crust causes a more gradual increase of Sn/Lg ratios for hypocenters within or below
26 the eclogite layer. We obtain the Sn/Lg ratios of 595 Tibetan earthquakes from 1998 to 2022 with nominal
27 (catalog) hypocentral depths >30 km and magnitudes >3.2 in five regions (west Tibet, southwest Tibet, south
28 Tibet, southeast Tibet, and Qiangtang). As predicted by our normal-mode synthetics, deep earthquakes in west
29 and south Tibet show Sn/Lg ratios that increase sharply as catalog depths approach the independently determined
30 receiver-function Moho. Numerous earthquakes with high Sn/Lg ratios and nominal depths around the reported
31 Moho are identified between the Karakoram fault and Altyn-Tagh fault (ATF) in west Tibet, which we attribute
32 to an eclogitized Indian lower crust extending north to the ATF. Impingement of this underthrust Indian slab
33 against the Tarim craton and consequent eclogite delamination or dripping may cause the observed below-Moho
34 seismicity which occupies a region 100 km across and 200 km along orogenic strike and extends 30–50 km
35 below published Moho depths. Similarly, dense seismicity spans the Moho and occupies a similar volume below
36 the Moho beneath the High Himalaya in south Tibet. The south Tibet Sn/Lg patterns may indicate an eclogitized
37 Indian layer beginning to delaminate or drip south of the Yarlung-Zangpo suture. Our southeast Tibet and
38 southwest Tibet Sn/Lg observations are less clear cut, perhaps due to less appropriate epicentral distances from
39 the available observing stations. The Qiangtang region of Tibet likely has sparse mid-to-lower-crustal
40 earthquakes, but no definitive below-Moho earthquakes. Our work expands the catalog of continental intraplate
41 earthquakes below the Moho by >100 events with $m_b > 3.2$, as well as identifying tens of $m_b > 3.2$ lower-crustal
42 events, so that Tibet fits neither an ideal crème-brûlée nor an ideal jelly-sandwich crustal-strength paradigm.
43 Two clusters of earthquakes that each span the Moho may be best explained by delamination or dripping of a
44 strong eclogitized lower crust into the upper mantle.
45

1. Introduction

The Tibetan plateau is the surface manifestation of the convergence between the Indian plate and the Eurasian plate, but ongoing complex deep-crustal and subcrustal tectonic processes (Shi et al., 2020; Klemperer et al., 2022) may hold the key to Tibet’s elevation and evolution. A path to understanding these lower-lithosphere processes is opened up by numerous intermediate-depth earthquakes (Chen and Molnar, 1983; Chen and Yang, 2004; Liang et al., 2008; Monsalve et al., 2006; Zhu and Helmberger, 1996), as shown in Fig. 1, whose hypocentral location (whether mantle or lower crust) is still under debate (Wang and Klemperer, 2021). The widely used “jelly-sandwich” continental-lithosphere rheology (Bürgmann and Dresen, 2008) with a weak lower crust and a brittle upper mantle was first envisioned in the belief that these deep earthquakes occurred within the mantle lithosphere (Chen and Molnar, 1983; Chen and Yang, 2004); such a model is supported by the observation of south Tibet earthquakes as being either in the upper crust or near the Moho (Liang et al., 2008; Monsalve et al., 2006). The opposed “crème brûlée” model (Bürgmann and Dresen, 2008) in which the lower crust is stronger than the upper mantle gains support from those who believe the Himalayan & Tibetan seismicity maybe exclusively lower-crustal (Jackson, 2002; Maggi et al., 2000). However, at least some Tibetan earthquakes have seismic phases clearly requiring they occurred beneath the Moho (Jiang et al., 2009; Wang and Klemperer, 2021; Zhu and Helmberger, 1996). Different ideas to explain Tibet’s deep earthquakes include underthrusting of cold brittle Indian lower crust together with its mantle lithosphere (Craig et al., 2012, 2020; Priestley et al., 2008), flexural stresses (Monsalve et al., 2009), eclogitization (Alvizuri and Hetényi, 2019; Schulte-Pelkum et al., 2019; Shi et al., 2018, 2020), and the extension of shallow faults into the upper mantle (Diehl et al., 2017; Michailos et al., 2021).

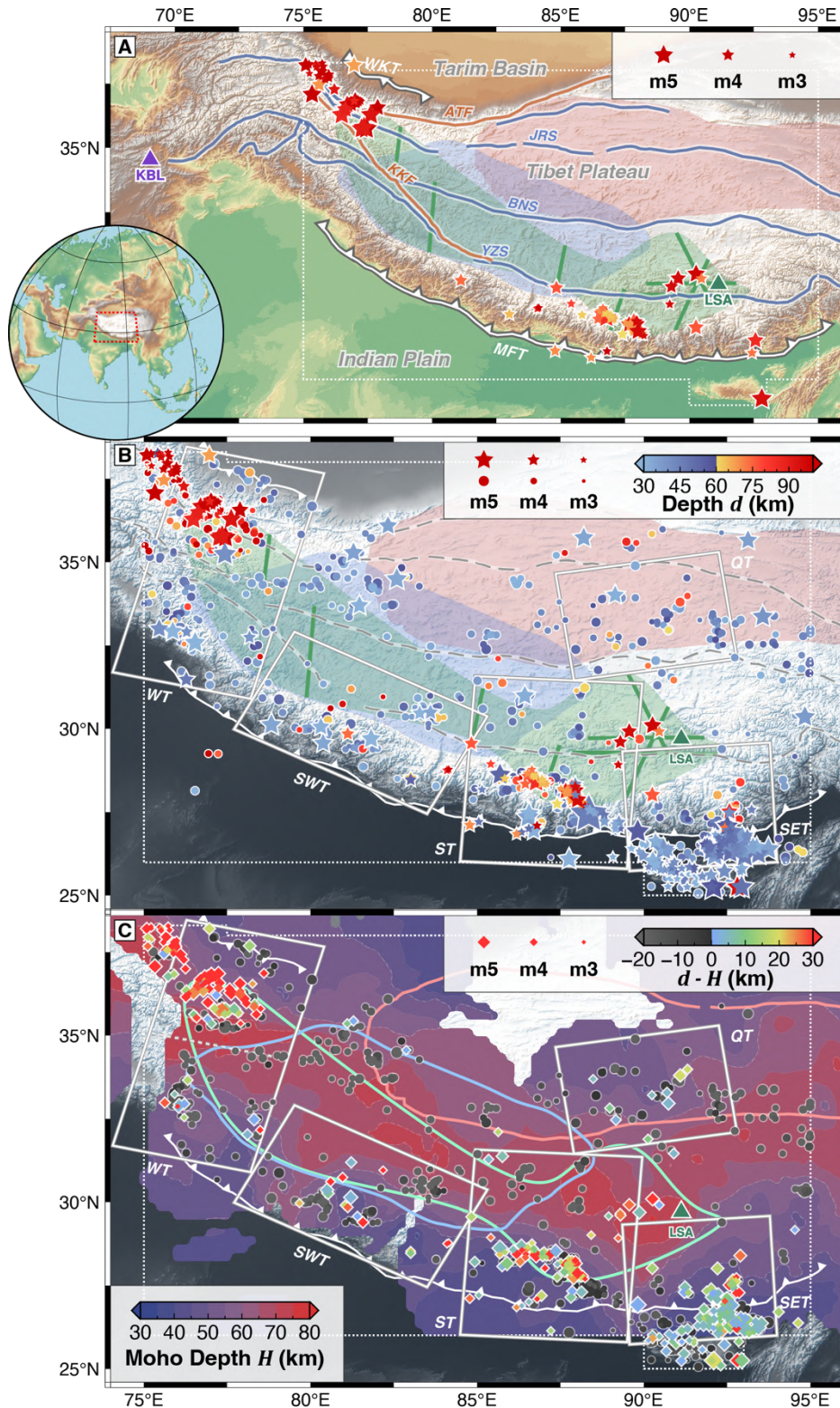
The debate on the cause of Tibetan intermediate-depth earthquakes is further complicated by the seismicity beneath Tibet’s south and northwest margins (Fig. 1A), a localization at odds with the believed regional extent of Indian underthrusting, flexural stress, eclogitization, and shallow faulting at specific places (Craig et al., 2012; Shi et al., 2020; Wittlinger et al., 2004b; Zhang et al., 2014). Previous assessments of the causes of Tibet’s near-Moho earthquakes have therefore either been restricted to the small areas in which such earthquakes have been found (Alvizuri and Hetényi, 2019; Monsalve et al., 2006; Schulte-Pelkum et al., 2005) or are ad hoc (e.g., that an extremely strong Indian crust would explain the absence of deep seismicity in central-west Tibet (Craig et al., 2012; Fig 1)). These puzzles motivate us to create & interpret a more complete catalog of the deep earthquakes across the entirety of Tibet.

The simplest method of detecting below-Moho earthquakes, the comparison between source depth and Moho depth, is limited in clarifying this debate, as double errors are introduced by the independent earthquake relocation and Moho determination (Priestley et al., 2008). Significant uncertainties exist in today’s Tibet Moho models (Xia et al., 2022; Zhao et al., 2020), and small earthquakes ($m_b < 4.5$) typically lack the well-recorded “depth phases” (pP , sP , etc.) at teleseismic distances that are often key to precise depth location (Craig et al., 2012). Our alternative approach aims to directly determine the layer in which an earthquake nucleates (above or below the Moho) based on waveform characteristics instead of on arrival times. We use the principle that earthquakes excite most of their energy in the waveguide in which they nucleate. The Lg and Sn wavetrains dominantly propagate in the crustal and upper-mantle waveguides respectively (Knopoff et al., 1973; Mousavi et al., 2014; Stephens and Isacks, 1977) so that mantle earthquakes have higher Sn/Lg amplitude ratios than crustal earthquakes (Wang and Klemperer, 2021). Our use of Sn/Lg ratios offers a way to distinguish below-Moho from above-Moho earthquakes independent of uncertainty in Moho depth or lithospheric wavespeed.

We use this Sn/Lg method to study 870 earthquakes from 1998 to 2021 across the entirety of Tibet (Fig. 1B). The lack of permanent Tibet stations prevents us from using a multiple-station analysis (Wang and Klemperer, 2021), so we develop a new single-station Sn/Lg method, using the statistics of very many earthquakes to overcome inherent uncertainties.

We first establish the theoretical and numerical basis for our Sn/Lg analysis, then describe our data, and apply our single-station method to five separate regions of Tibet: west Tibet (WT), south Tibet (ST), southeast Tibet (SET), southwest Tibet (SWT), and Qiangtang (QT) (Fig. 1B). We present Sn/Lg results and analysis for

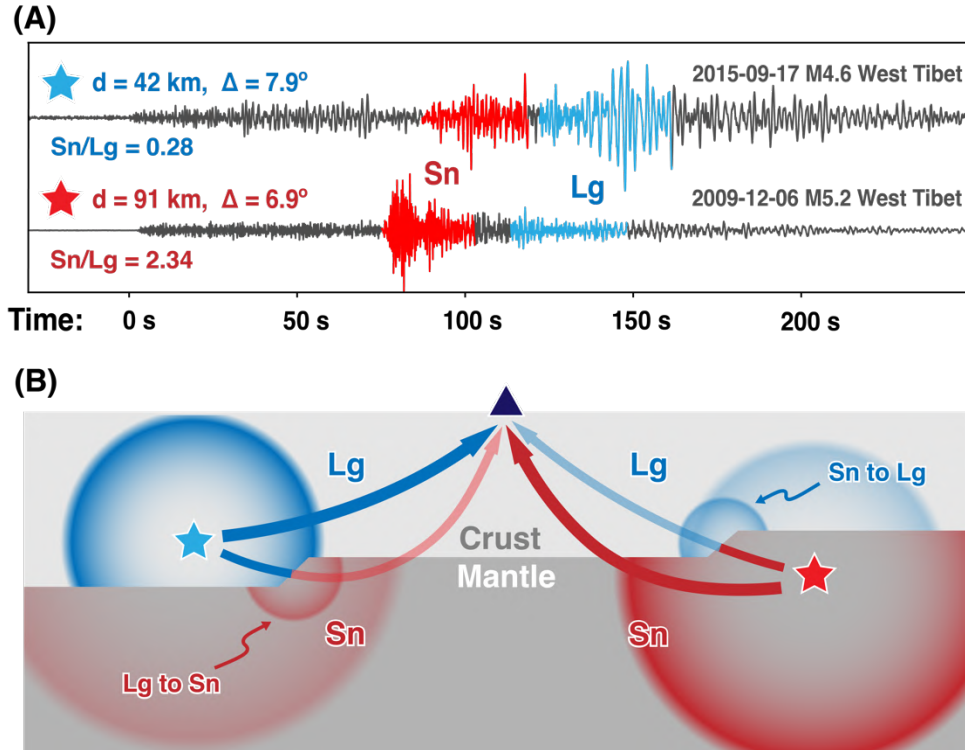
101 WT in section 3, and along the Himalaya arc (ST, SET, SWT) in section 4. Analysis of the S_n/L_g results for
 102 QT is provided in supplementary material. Limitations caused by model heterogeneity, catalog uncertainty, and
 103 regional attenuation are discussed in section 5. Finally, we interpret Tibet's rich near-Moho earthquake catalog
 104 as associated with the loss of lower-crustal mafic eclogites from the crust into the mantle.
 105



106

107
 108
 109
 110
 111
 112
 113
 114
 115
 116
 117
 118
 119

Fig. 1. (A) Tibet topography and tectonic boundaries. White dotted box and red dash box (global map) correspond. Stars are the earthquakes below 30 km located by the Global CMT project, ISC-GEM project, or relocated by specific studies (see section 3.1), colored by hypocentral depth & sized by magnitude. Two triangles are the two permanent stations (IC.LSA and IU.KBL) used in this study. Pink transparent overlay is the high S_n attenuation zone in northern Tibet (McNamara et al., 1995). Blue transparent overlay is the Tibet deep aseismic zone (Craig et al., 2012). Green overlay encompasses seismic profiles (solid green lines) along which eclogite has been proposed (Shi et al., 2020; Wittlinger et al., 2004a, 2004b, 2009). Sutures, thrusts, and faults from Taylor and Yin (2009): MFT: Main Frontal and WKT: West Kunlun thrusts; YZS: Yarlung-Zangpo, BNS: Bangong-Nujiang, and JRS: Jinsha River sutures; KKF: Karakoram and ATF: Altyn-Tagh faults. **(B) Tibet earthquakes with catalog depth > 30 km, 1998-2022.** White solid frames are the five regions analyzed separately in this study. **(C) Tibet Moho depths from receiver functions (Xia et al., 2022).** Colored diamonds and grey dots are earthquakes with nominal depths beneath & above the receiver function Moho, respectively. Other legends are the same as (a) and (b).



120
 121
 122
 123
 124
 125
 126
 127
 128
 129
 130
 131
 132
 133
 134
 135
 136
 137
 138
 139

Fig. 2. (A) Examples of S_n and L_g selection (tangential component of two nearby west Tibet earthquake recorded at Kabul) and (B) schematic mechanisms of S_n and L_g amplitude differentiation. A crustal earthquake (blue star) excites stronger seismic waves in the crust (L_g) and weaker waves in the upper mantle (S_n) (left), and vice versa for an upper-mantle earthquake (red star, right). S_n and L_g conversions are possible at Moho ramps: L_g may be blocked travelling from thicker to thinner crust (left) and S_n when travelling from thinner to thicker crust (right) (Kennett, 1986).

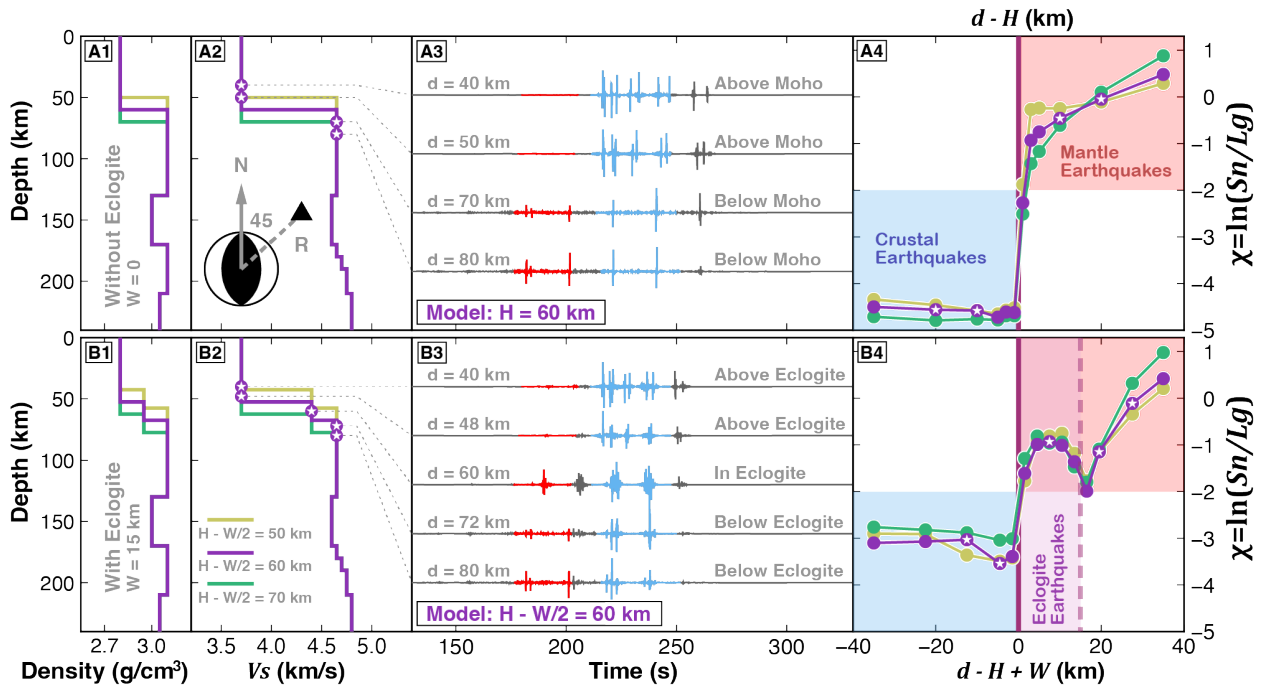
2. Theoretical and numerical base of S_n/L_g ratio analysis

Both the S_n and L_g phases, that are respectively largely confined to upper-mantle & crustal waveguides, can be understood by mode theory (Knopoff et al., 1973; Wang and Klemperer, 2021) or multiply reflected ray theory (Kennett, 1986; Press and Ewing, 1952). In this study, we restrict ourselves to the Love-mode interpretation of the transverse component of seismograms. We follow Wang and Klemperer (2021) in applying Generalized Eigenproblem Spectral Collocation (GESOC, Denolle et al., 2012) to calculate and sum Love-wave eigenvectors to get the synthetic waveforms. The vertical variation of the eigenvectors shows that S_n and L_g concentrate their energy in the upper mantle and the crust, respectively, enabling Wang and Klemperer (2021) to establish the theoretical basis for a practical S_n/L_g analysis by synthesizing seismograms for oceanic, cratonic, and Tibetan wavespeed models, and for a variety of focal mechanisms and depths.

140
 141
 142
 143
 144
 145
 146
 147
 148
 149
 150
 151
 152
 153
 154
 155
 156
 157
 158
 159

Here we show synthetics for simplified Tibet models with a thick single-layer crust above an upper-mantle lid and low-velocity zone (Fig. 3A, Zhao et al., 1991). We also calculate synthetics for doublet models with a 15-km-thick high-shear-velocity (“4.x” km/s) base-crustal layer (Fig. 3B). In south Tibet, a lower-crustal doublet or pair of receiver-function converters at the Moho and 10-20 km shallower (Henry et al., 1997) has been widely interpreted as eclogitized mafic Indian lower crust (Kind et al., 2002). Our doublet models have a $W = 15$ km thick lower-crustal layer (Fig. 3B1&2) with wavespeed and densities appropriate for eclogite (Shi et al., 2020; Wittlinger et al., 2009). The Moho depth (the base of the eclogite layer for the doublet models) is defined as H and varies from 50–70 km for our single-Moho models (and 62.5–82.5 km for our doublet models). We model a compressional double-couple source at different depths d ranging from 35 km above to 35 km below the Moho (Fig. 3A, or doublet top in Fig. 3B), as recorded at 800 km in the direction 45° from the source’s strike.

We use a Gaussian source time function (standard deviation 2 Hz) and calculate 100 modes of the eigenfunctions before bandpass filtering 0.5-4 Hz. The Sn and Lg windows are defined using a ray-theory approximation, the known earthquake depth, and a uniform crust and mantle with Moho depth (H) of 70 km to mimic the real-world situation where we do not know the Moho depth (Supplementary Material S1). Hence our Sn window can include energy (e.g., trapped in the crustal eclogite layer) that is not strictly Sn that is defined as travelling in the mantle. We measured amplitudes of the Sn and Lg phases as the root mean square of the signal within their time windows (Mousavi et al., 2014).



160
 161
 162
 163
 164
 165
 166
 167
 168
 169
 170

Fig. 3. Source & model parameters and resulting synthetics. (A1-2) Densities and s-wave velocities of the sharp-Moho models after Earth-flattening transform (Supplementary Material S2). Yellow, purple, and green lines represent Moho depths of $H = 50$ km, 60 km, and 70 km, respectively. The focal mechanism and the triangle in (A2) represent the source & receiver; synthetics are for $R = 800$ km. Purple dots with stars marks the depths of the sources whose seismograms for the purple model are shown in (A3). **(A3) Synthetic waveforms for earthquakes at different depths in the model with a 60 km Moho depth.** Red and blue trace segments are the Sn and Lg windows, calculated as in Supplementary Material S1. **(A4) $\ln(Sn/Lg)$ vs $(d - H)$** (source depth minus Moho depth) for sources from 35 km above to 35 km below the Moho in the sharp-Moho models. **(B1-4) as (A1-4) but for models with 15-km eclogitized lower crust.**

171
 172
 173

For the simple Moho models, increasing source depth leads to a step increase of Sn/Lg ratio at the Moho depth H , followed by a gradual increase at larger depths (Fig. 3A). For the doublet models, a similar sharp increase of Sn/Lg ratio at the top of the eclogite layer is followed by a decrease at the bottom of the layer and

174 then a rebound. The high S_n/L_g ratios in the eclogite layer can be explained by the ray-theoretical deeper mirror
175 source formed by the reflective base of eclogite, whose effect vanishes for sources below the eclogite layer. For
176 all our models, we can make a binary classification with earthquakes below the Moho or within the doublet
177 having $\chi = \ln(S_n/L_g) > -2$ and the crustal earthquakes above the doublet having $\chi \leq -2$ (pink and blue
178 regions in Fig. 3 A4, B4).

179
180 Previous studies have shown the relative lack of dependence of S_n/L_g on focal mechanism and receiver
181 azimuth or distance (Wang and Klemperer, 2021). Our GESC synthetics do not model geometric spreading,
182 attenuation, or scattering and in consequence synthetic S_n/L_g ratios are systematically smaller than observed in
183 real data (see sections 3 and 4). This systematic difference does not impede our single-station S_n/L_g analysis, as
184 a threshold $\chi (= \ln(S_n/L_g))$ should also exist in the observations albeit larger than the threshold $\chi = -2$ seen
185 in the synthetics.

186 187 188 **3. Data processing**

189 190 *3.1 Data selection*

191
192 We select all earthquakes within 26° – 38° N and 75° – 95° E and depth range 30–150 km (20–150 km for
193 southeast Tibet and northeast India) from 1998 to 2021 with $m \geq 3.5$ in the USGS-PDE catalogue (PDE, 2022),
194 and $m \geq 3.2$ in the ISC-GEM (Global Instrumental Earthquake, Bondár et al., 2015) and Global CMT
195 (Centroid-Moment-Tensor, Dziewonski et al., 1981) catalogues, and previous relocation studies (Alvizuri and
196 Hetényi, 2019; Baur, 2007; Bloch et al., 2021; Craig et al., 2012; Diehl et al., 2017; Michailos et al., 2021;
197 Monsalve et al., 2006; Parija et al., 2018). Earthquakes from sources other than the USGS-PDE are classified as
198 “better-located” events in this study and are plotted as stars (Fig. 1A and B) in contrast to events only in the PDE
199 catalog shown as circles. Our initial earthquake catalog contains 870 earthquakes across the Himalaya and Tibet
200 (Fig. 1B and C) for which seismic waveforms recorded at Lhasa (IC.LSA, 1998–present) and/or Kabul (IU.KBL,
201 2007–present) were obtained from IRIS. Further details on building our initial catalog are provided in
202 supplementary materials S3.

203 204 *3.2 The practical single-station method*

205
206 For all 870 earthquakes we calculate S_n & L_g windows exactly as described for the synthetics (section 2.1).
207 For the window calculation, rather than adjusting the Moho depth for each earthquake, we fix the Moho depth
208 at 70 km as a crude average depth between source and receiver. We apply a 0.5–4 Hz bandpass for the L_g
209 window and a 1–4 Hz bandpass for the S_n window and calculate the signal-to-noise ratios (SNR) of both phases
210 (supplementary materials S4). We discard earthquakes for which both SNR_{L_g} and $SNR_{S_n} < 3$, and for the
211 remaining data calculate S_n/L_g ratios and uncertainties, using the measured SNR (supplementary material S4).
212 We then finally approximately correct the S_n/L_g ratios for geometric spreading effects (Fan and Lay, 2003;
213 Yang et al., 2007) (supplementary material S5).

214
215 For each earthquake we know the catalog depth d , and we can estimate Moho depth H from published Moho
216 maps (e.g., Xia et al., 2022; Zhao et al., 2020). Here we use a recent compilation of receiver-function (RF) Moho
217 depths to obtain H (Xia et al., 2022) and plot $d - H$ for every earthquake (Fig. 1C).

218
219 Our first-order observation is that although earthquakes with catalog depths ≥ 30 km are scattered across
220 the entire Tibet Plateau, most of them that are nominally below the receiver-function Moho lie broadly parallel
221 to the Himalaya arc, largely between the Main Frontal Thrust (MFT) and the Yarlung Zangpo suture (YZS), but
222 continuing north to the Altyn Tagh Fault (ATF) in northwest Tibet, and continuing south of the MFT in southeast
223 Tibet. Five smaller regions (solid white frames in Fig. 1B and C) capture most of these near-Moho earthquakes:
224 west Tibet (WT), southwest Tibet (SWT), south Tibet (ST), southeast Tibet (SET), and Qiangtang (QT),
225 respectively. We focus on the records from Kabul in WT and SWT and the records from Lhasa in ST, SET,
226 SWT, and QT. We next plot S_n/L_g amplitude ratios vs $(d - H)$ for each region. Based on our synthetics

(Section 2.1), S_n/L_g is dominantly controlled by hypocentral distance above or below the Moho, so using $d - H$ instead of d largely removes the effect of Moho topography. We project these earthquakes, with their S_n/L_g ratios, onto regional cross-strike lithospheric profiles to help understand the tectonic setting.

4. S_n/L_g results for Tibet earthquakes

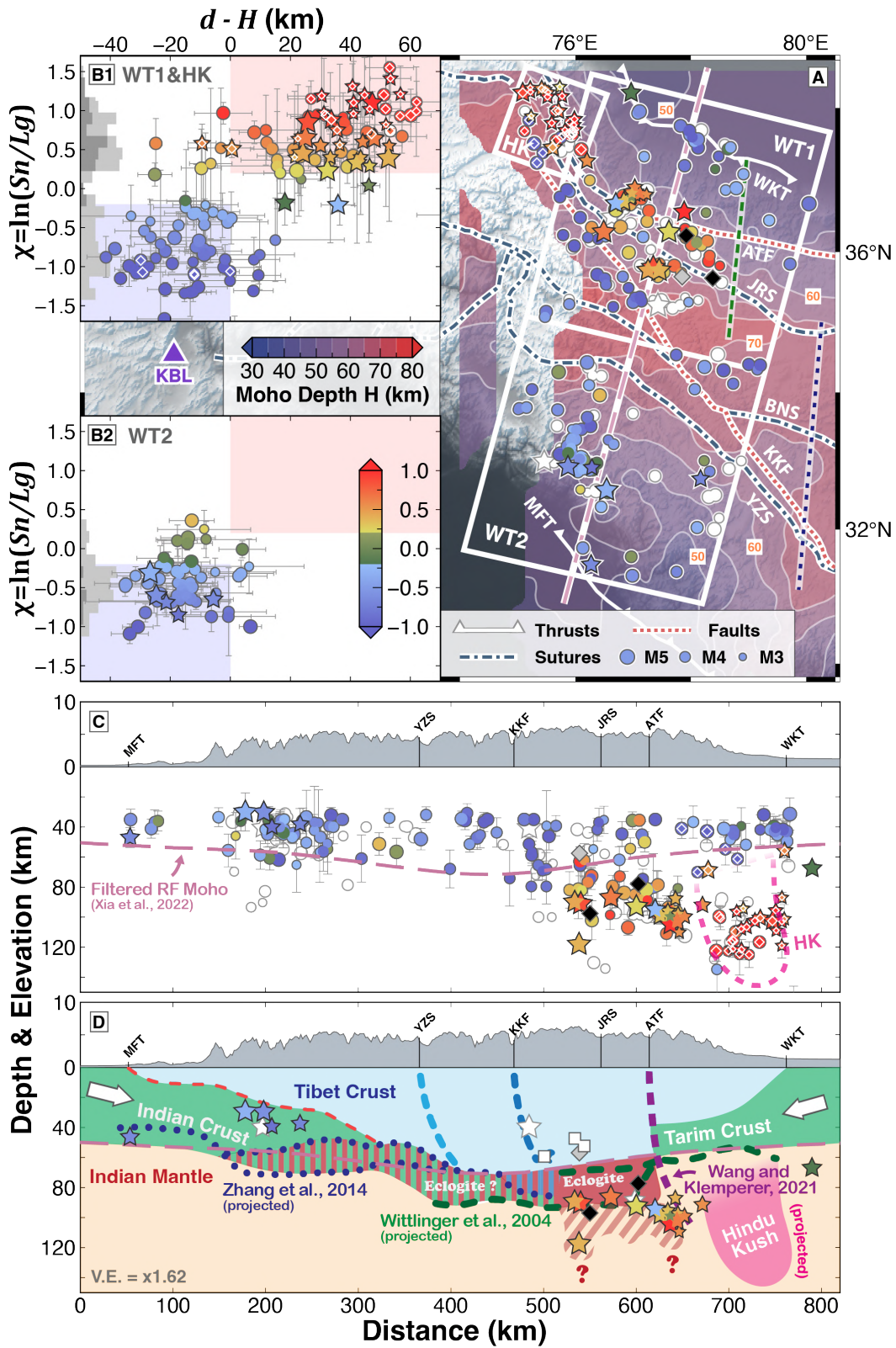
4.1 West Tibet (WT)

Chen and Yang (2004) claimed that four earthquakes beneath the Jinsha River Suture in northwest Tibet originated in the mantle; but additional teleseismic analyses of these and six other events could not distinguish whether these hypocenters, at ~ 80 – 100 km depth, are above or below the Moho (Craig et al., 2012; Priestley et al., 2008). In this complex area, we follow previous work (Craig et al., 2012; Priestley et al., 2008) in separating the intermediate-depth earthquakes caused by the Hindu Kush subduction (Fig. 4 box HK) from the deep earthquakes of interest in this paper that are associated with Indian-Asia convergence. Huang et al. (2011) showed with local recordings that at least some of the seismicity nucleated in the lower crust, and Wang and Klemperer (2021) used array S_n/L_g analysis of regional recordings to demonstrate that at least two, and very probably 12, hypocenters were sub-crustal. We measured S_n/L_g for 196 earthquakes in our west Tibet (WT) area from 2007 to 2021 from the IU.KBL station (Fig. 4). Starred earthquakes include better-located events from previous studies (Bloch et al., 2021; Craig et al., 2012; Parija et al., 2018) and ISC-GEM & GCMT catalogs (Bondár et al., 2015; Dziewonski et al., 1981). We describe the WT earthquakes in two subregions, WT1 and WT2 (Fig. 4A), and discuss their significance in section 5.1.

For the WT1 region with prolific deep seismicity (roughly southern Tarim to Bangong-Nujiang suture), there is on average a tripling of S_n/L_g ratio between earthquakes below and above Xia et al.'s (2022) Moho, as predicted by our synthetics. An intermediate zone of $\chi = \ln(S_n/L_g) \in (-0.2, 0.2)$ with almost no earthquakes separates the below-Moho from the above-Moho earthquakes (see color bar and red & blue boxes in Fig. 4B). For tectonic interpretation we separate the region HK (Fig. 4, dots with diamonds embedded), an area identified as a continuation of the Hindu Kush subduction (Bloch et al., 2021; Priestley et al., 2008), from the main WT zone, even though these HK earthquakes all meet our expected (S_n/L_g) vs ($d - H$) relation. Excluding these HK earthquakes, we find no definitive mantle seismicity north of the ATF.

Earthquakes in the WT2 region (roughly Bangong-Nujiang suture to Main Frontal Thrust) are mostly located in the crust, with the few that are within uncertainty below the Moho all having “crustal” S_n/L_g ratios (Fig. 4B2). All three better-located events are in the crust and have low S_n/L_g ratios. A few earthquakes apparently within the crust, that have intermediate or mantle S_n/L_g ratios, are in the region south of the Yarlung-Zangpo suture where Zhang et al. (2014) observed a Moho doublet and suggested an eclogite lower-crustal layer.

Using to the Xia et al. (2022) RF Moho, for the whole WT region (including HK), 168 earthquakes (supplementary material S6) have S_n/L_g ratios matching their reported depths, and 19 may match within error. Just 9 earthquakes have S_n/L_g ratios that fail to match their ($d - H$) values, but we do not know whether this failure represents a breakdown of our S_n/L_g method, or larger-than-quoted errors in earthquake & Moho depth measurements. Thus, our single-station estimation of whether an earthquake is above or below the Moho appears to be correct for 86% of all 196 events. We conclude that S_n/L_g ratios can statistically separate above-Moho and below-Moho earthquakes with confidence despite several potentially confounding issues (e.g., variable attenuation & Moho topography between source & receiver; unknown focal mechanism; scattering of vertical and radial energy on to the transverse component). (For discussion of the effect of Moho topography see supplementary material S7).



278
279
280
281
282

Fig. 4. (A) S_n/L_g amplitude ratios in west Tibet (WT) from recordings at Kabul (KBL). Solid white frames (rectangle) show the WT region, separated into subregions WT1, WT2, and area HK (Hindu Kush), superimposed on Moho depth (Xia et al., 2022). Colored dots show the S_n/L_g ratios for each earthquake. Colored stars are events with better defined depths (see section 3.1). Pink

283 dashed line: line of section in (C) and (D). White circles and stars are earthquakes for which Sn/Lg ratios are not available because
284 of low SNR or missing data. White diamonds mark earthquakes in the HK region of well-accepted continental subduction (Kufner
285 et al., 2016). Two black and one grey diamonds mark the earthquakes previously demonstrated to be below-Moho (black) and one
286 above-Moho (gray) by Wang and Klemperer (2021). Blue dotted and green dashed lines are Moho interpreted by Zhang et al. (2014)
287 and Wittlinger et al. (2004b). Faults labeled as in Fig. 1A. **(B1-2) $\ln(Sn/Lg)$ vs $(d - H)$ plots for the WT1 and WT2 regions.**
288 Color bar is chosen based on natural breaks in the distribution of Sn/Lg values, as shown in grey histogram on left axis. Red, blue,
289 and green segments of the color bar represent Sn/Lg of probable below-Moho earthquakes (pink box), probable above-Moho
290 earthquakes (light blue box), and intermediate values. **(C) Cross-section of Sn/Lg ratios along profile A.** Pink dashed line is the
291 filtered RF Moho (Xia et al., 2022, supplementary material S8). **(D) Cartoon tectonic interpretation, showing only ‘better-
292 located’ events (stars).** Blue dotted and green dashed lines mark the Moho and doublet layers from Zhang et al. (2014) and
293 Wittlinger et al. (2004b) respectively. Boundary between green Indian crust and cyan Tibetan crust (Main Himalayan Thrust, red
294 dashed line) from Gao et al. (2016). Purple dashed line: possible continuation of ATF below the Moho (Wang and Klemperer,
295 2021). White squares: projected WT lower crustal earthquakes relocated by Huang et al. (2011).

297 298 4.2 Himalaya Arc

299
300 We apply the same analysis to our south, southeast, and southwest Tibet (ST, SET, SWT) regions in
301 sequence from regions with the best constraints (ST) to the fewest data (SWT).

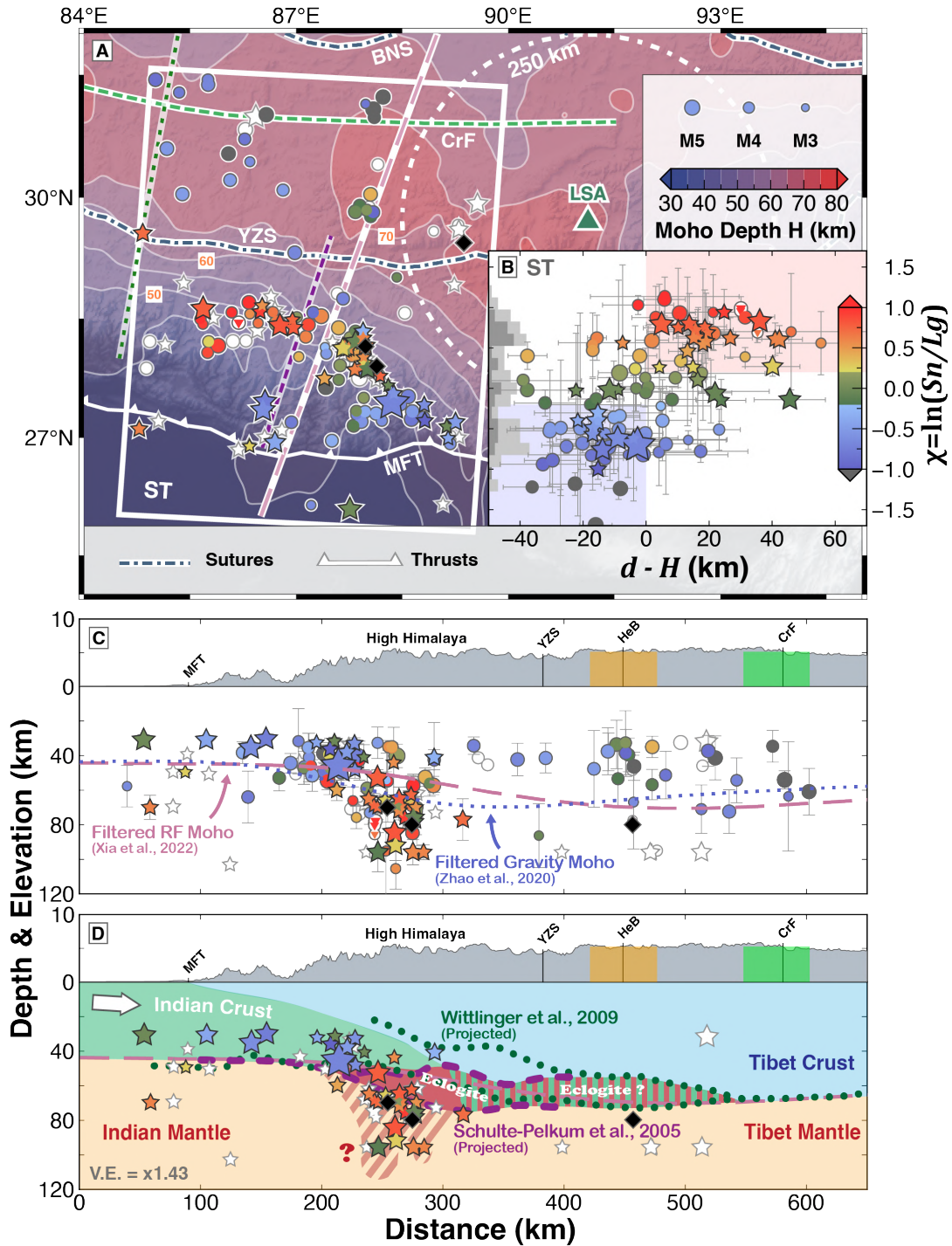
302 303 4.2.1 South Tibet (ST)

304
305 The Higher Himalayan and Tethyan Himalayan from ~ 86 - 89°E are rich in near-Moho seismicity (e.g.,
306 Craig et al., 2012; Diehl et al., 2017; Liang et al., 2008; Michailos et al., 2021; Monsalve et al., 2006). The 1991-
307 1992 Tibet PASSCAL experiment recorded three earthquakes identified from waveform analysis of
308 local/regional recordings (Zhu and Helmberger, 1996) and corroborated using Sn/Lg analysis (Wang and
309 Klemperer, 2021) as having occurred below the Moho. An additional group of six tiny earthquakes have been
310 shown to be below-Moho by their S -minus- P travel time compared to receiver functions recorded at the same
311 temporary station (Schulte-Pelkum et al., 2005), but their magnitudes (< 2.9) are below our cut-off of $m_b = 3.2$.
312 We measure Sn/Lg ratios of 113 earthquakes in our ST region recorded at Lhasa from 1998 to 2022 (Fig. 5).

313
314 Recordings at IC.LSA from ST show a steady increase of Sn/Lg ratios with respect to depth, and a step
315 change near Xia et al.’s (2022) receiver-function Moho (Fig. 5B), just as for Kabul recordings from WT (Fig.
316 4). Using identical criteria as for WT we see the same binary distribution with reference to the Moho, correctly
317 categorizing almost all the events with more reliable depths (stars in Fig. 5). Most of the high Sn/Lg earthquakes
318 are in a previously noted near-Moho seismogenic zone (Diehl et al., 2017; Liang et al., 2008; Monsalve et al.,
319 2006), but whereas previous studies could not typically distinguish crustal from mantle earthquakes because of
320 uncertainties in both earthquake depth and Moho depth, our Sn/Lg method shows this seismogenic zone crosses
321 the Moho, nucleating earthquakes both in the crust and in the mantle (Fig. 5 B, C). A few deep earthquakes with
322 large depth uncertainties show low Sn/Lg ratios (top left quadrant, Fig. 5B), and at ~ 20 km below the Moho
323 several well-located earthquakes show intermediate Sn/Lg ratios (bottom right quadrant, Fig. 5B), possibly
324 corresponding to the lower Sn/Lg ratios observed in our synthetics for earthquakes at or just below the base of
325 an eclogite layer.

326 327 4.2.2 Southeast Tibet (SET)

328
329 In contrast to WT and ST, possible mantle earthquakes north of the trace of the MFT in southeast Tibet
330 (SET) are quite rare, though proximity to Lhasa means that we cannot use Sn/Lg ratios to properly examine a
331 number of candidate deep earthquakes (~ 250 km is the minimum distance beyond which Sn and Lg phases
332 become well developed (Mousavi et al., 2014) and clearly differentiated in time (Fig. S1-2)). Since the RF Moho
333 compilation of Xia et al. (2022) does not include studies in NE India, south of 26.5°N we use data from Mitra et
334 al. (2018), Fig. 6A). We measure Sn/Lg ratios at Lhasa for 172 earthquakes from SET, of which 79 are “well-
335 located”, mostly from the GANSSER catalog (Diehl et al., 2017). India south of the Main Frontal Thrust has
336 crust only ~ 40 km thick, so here our catalog includes all earthquakes with nominal depths > 20 km.



338

339

340 **Fig. 5. (A) Spatial distribution of $\ln(Sn/Lg)$ ratios in south Tibet (ST) measured from recordings at IC.LSA (green triangle).**

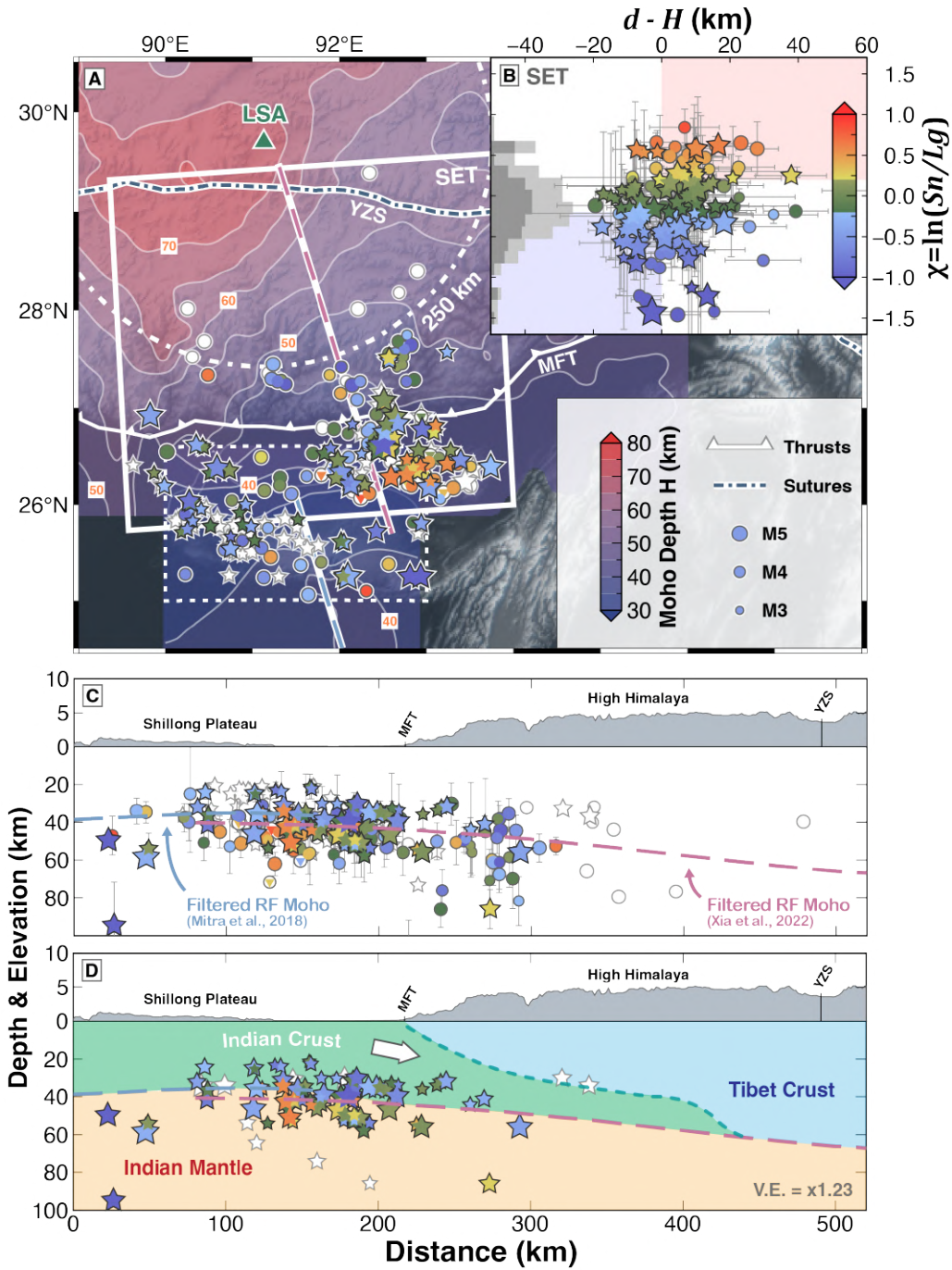
341 Legend as in Fig. 4. White dots with colored triangles embedded are the earthquakes from the USGS-PDE catalog without depth

342 uncertainties (likely poor located). Black diamonds mark the three earthquakes previously demonstrated to be in the mantle (Wang

343 and Klemperer, 2021; Zhu and Helmberger, 1996). White earthquake symbols are <250 km from Lhasa (shown by the white dot-344 dashed circle), too close for reliable $\ln(Sn/Lg)$ measurements; or as in Fig. 4 represent low SNR events or missing data. Dashed green345 line is the crustal front (CrF, Nábělek et al., 2009). **(B) $\ln(Sn/Lg)$ vs $d - H$ plots for the ST region. (C) Cross-section of $\ln(Sn/Lg)$** 346 **ratios along the profile in (A). Dotted line: gravity Moho (Zhao et al., 2020). HeB denotes the $^3\text{He}/^4\text{He}$ boundary and possible**347 **mantle suture (Klemperer et al., 2022). (D) Cartoon**

348
 349
 350

tectonic interpretation, showing only 'better-located' events (stars). Dotted green lines and dashed purple lines mark the Moho and receiver-function doublets (Schulte-Pelkum et al., 2005; Wittlinger et al., 2009).



351
 352
 353
 354
 355
 356
 357
 358

Fig. 6. (A) Spatial distribution of Sn/Lg ratios in southeast Tibet (SET). Dashed box uses receiver-function Moho of Mitra et al. (2018). (B) $\ln(Sn/Lg)$ vs $d - H$ plots for the SET region. Legends as in Fig. 5B. (C) Cross-sectional view of the Sn/Lg ratios along the offset profiles in (A). Mint-green dashed line marks the projected MHT extension (Grujic et al., 2011). Blue dashed line is the filtered RF Moho from Mitra et al. (2018). Legends as in Fig. 4 & 5. (D) Cartoon tectonic interpretation, showing only 'better-located' events (stars). Boundary between green Indian crust and cyan Tibetan crust (Main Himalayan Thrust, mint dashed line) from Grujic et al. (2011).

359
360
361
362
363
364
365
366
367
368
369
370
371
372
373
374
375
376
377
378
379
380
381
382
383
384
385
386
387
388
389
390
391
392
393
394
395
396
397
398
399
400
401
402
403
404
405
406
407
408
409
410
411

SE Tibet shows a continuous gradation of S_n/L_g ratios from values that in west Tibet and south Tibet are clearly above Moho to clearly below Moho. In SET there is a maximum in the number of earthquakes very close to Moho depths (Fig. 6B), as opposed to the minima observed in the equivalent histograms for WT and ST (Figs. 4B, 5B). Although the receiver-function Moho map in SE Tibet may have larger errors than elsewhere in Tibet, uncertainties in $d - H$ cannot explain the gradational S_n/L_g values nor the unusual spatial location of the near-Moho seismicity. However, unlike the cases in WT and ST, essentially all the near-Moho seismicity in SET is shallower than the 70 km Moho beneath the recording station Lhasa, leading to S_n blockage that will vary with the source depth to potentially smear out measured S_n/L_g ratios into a continuum (Fig. 2B). The “well-located” earthquakes from 50-90 km below the Shillong Plateau with unexpectedly low S_n/L_g may be good examples of S_n/L_g being reduced by the north-dipping Moho ramp beneath the High Himalaya.

4.2.3 Southwest Tibet

Our southwest Tibet region has much less deep seismicity than further west (WT) or east (ST) and extends north into a region of “no deep seismicity” (Craig et al. 2012; blue region in Fig. 1B and C). Our SWT is approximately equidistant from Lhasa and Kabul, allowing us to compare recordings from the two stations.

We obtained the S_n/L_g ratios of 47 earthquakes from 2000 to 2019 for LSA and 30 earthquakes from 2007–2022 for KBL (Fig. 7), of which 19 were recorded at both stations (supplementary materials S9). Because of the long distance to both stations (~700–1300 km, Fig. S9-1), the S_n/L_g ratios tend to have much larger uncertainties than results for WT and ST. We cannot observe any explicit binary classification in either of the S_n/L_g vs $d - H$ plots (Figs. 7A2, 7B2), as most of the recorded earthquakes locate in the crust. Our LSA and KBL analyses both successfully classify most of the crustal earthquakes as low S_n/L_g ($S_n/L_g < 1$) using criteria we developed in WT and ST. The few earthquakes with low S_n/L_g and depths well below the Moho have large depth uncertainty. KBL recorded no earthquakes with high S_n/L_g . LSA recorded a few deep earthquakes with high S_n/L_g ratios but only one well-located event (W1) is also well-recorded at KBL and there has much lower S_n/L_g . We suggest that differences in crustal attenuation between raypaths from the SWT region to KBL (largely across Indian craton) and to LSA (entirely across Himalaya and Tibet) likely cause the very different S_n/L_g measured at the two stations for W1 (Supplementary Fig. S7). With <50 earthquakes in SWT (less than half the number in WT, ST or SET), we cannot tell whether WT1 and the nearby cluster of earthquakes from km 80–200 (Fig. 7A3) cross from the lower crust into the upper mantle; yet the dimensions of this cluster and its location beneath the highest Himalayan topography, resemble the Moho-crossing cluster in ST (Fig. 5C).

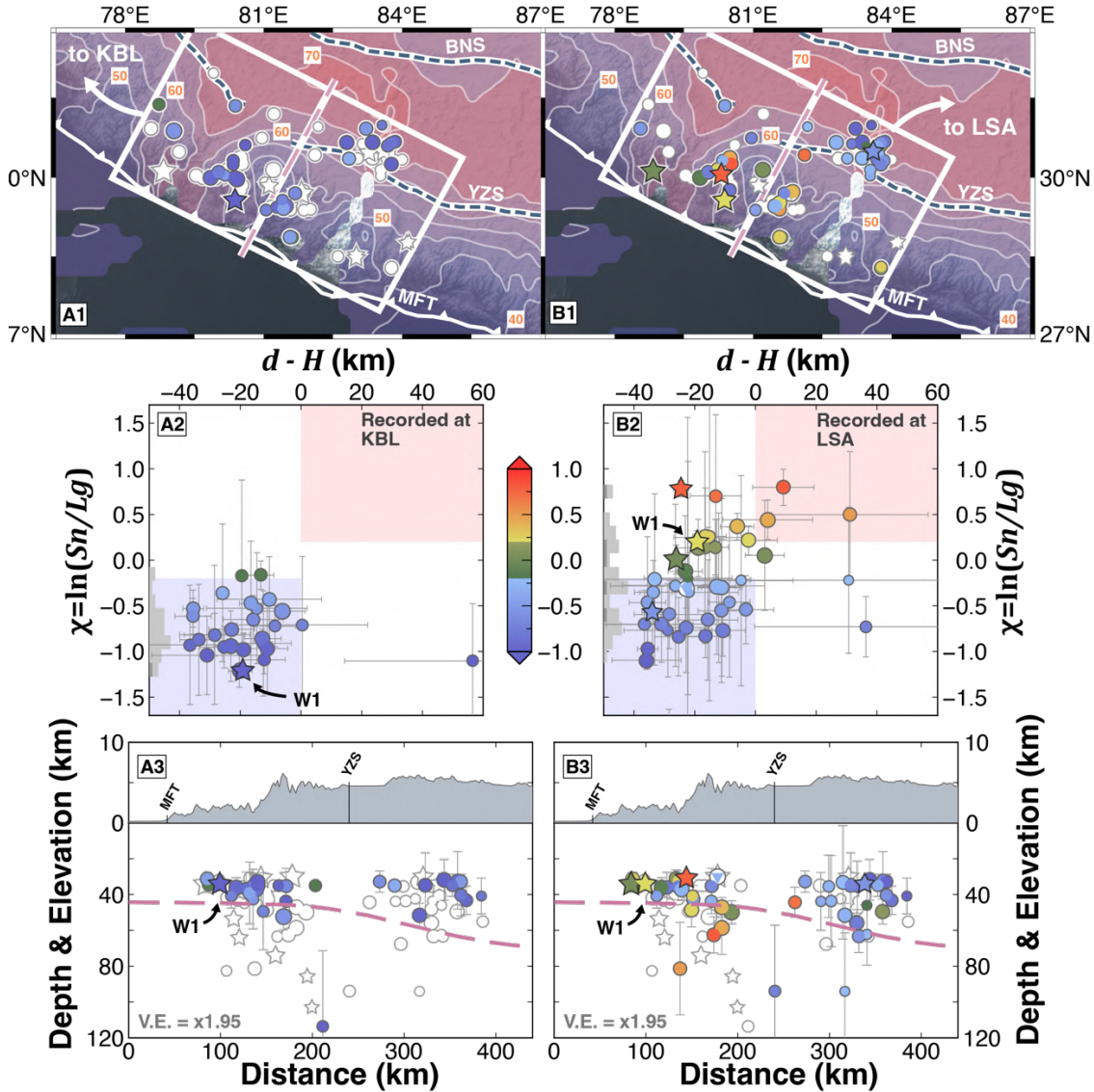
4.2.4 Qiangtang Tibet

We studied 56 earthquakes with nominal catalog depths from 30-80 km, but conclude from their S_n/L_g ratios that none of these earthquakes originated in the mantle (supplementary material S10).

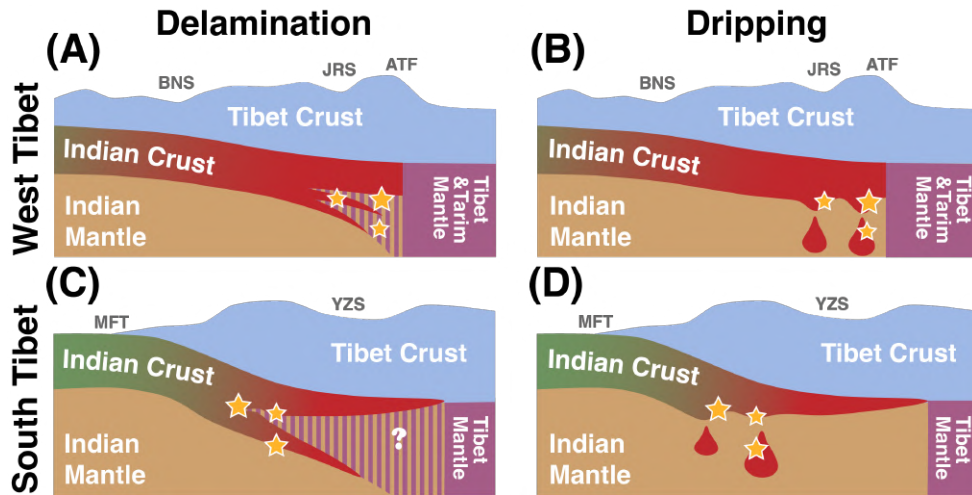
5. Discussions and Tectonic Implications

Our observations show that our single-station S_n/L_g method is able to characterize earthquakes down to magnitude 3.2 as nucleating above or below the Moho. In west Tibet we find pronounced breaks in the distribution of S_n/L_g ratios that lets us confidently identify 50 earthquakes (and likely 72) as nucleating below the Moho, a huge increase over the 12 previously identified (Wang and Klemperer, 2021) (Supplementary Table S6-2). In south Tibet we are similarly able to show at least 25 earthquakes (likely 40) nucleated below the Moho, compared to 9 previously known (Schulte-Pelkum et al., 2019; Wang and Klemperer, 2021). However, our southeast and southwest Tibet observations have less clear S_n/L_g depth separations, likely because SET is too close to the observing station, causing overlap of S_n & L_g windows (supplementary material S1), and because SWT is too far from KBL & LSA, leading to low SNR.

412 Our systematic search for intermediate-depth earthquakes across the entire Tibet plateau confirms previous
 413 belief that there are just two isolated areas where below-Moho earthquakes are common today (Craig et al., 2012;
 414 Priestley et al., 2008): beneath the Jinsha River Suture in northwest Tibet (Fig. 4) and beneath the southern
 415 Tangra-Yumco and Pumco-Xainza rifts in the southern Tethyan Himalaya (Fig. 5). Our study of two additional
 416 areas is hampered by less-certain Moho depths and proximity to LSA (SET) and too few high-quality recordings
 417 (SWT). The agreement between even relatively poor USGS-PDE hypocentral depths and our S_n/L_g
 418 characterization of earthquake depths implies that at least some of the lower-crustal depth-estimates found in all
 419 areas of Tibet, are likely also reliable (Fig. S3-2). Hence, $m \geq 3.2$ earthquakes likely exist throughout the crust
 420 of Tibet, perhaps even including the Qiangtang (Fig. S10), albeit in much smaller numbers than in the shallow
 421 crust.
 422



423
 424
 425 **Fig. 7. (A1) Spatial distribution of S_n/L_g ratios in southwest Tibet as recorded at KBL. (A2) $\ln(S_n/L_g)$ vs $d - H$ for SWT**
 426 **recorded at KBL. (A3) Cross-section of S_n/L_g ratios along the profile in (A1). W1 is the only well-located earthquake recorded**
 427 **at both Kabul and Lhasa. (B1-3) S_n/L_g ratios recorded at LSA. Legends as in Fig. 4, 5, and 6.**
 428
 429



430
431
432 **Fig. 8. Cartoons of deep-crustal and below-Moho earthquakes** beneath west Tibet (A)(B) and south Tibet (C)(D), drawn to
433 show Indian lower-crustal delamination (sheet-like rollback) (A, C) or dripping (circular in horizontal cross-section) (B, D).
434 Fault abbreviations as in Fig. 1.
435

436 In both regions of abundant below-Moho earthquakes, our catalog suggests a rich sequence from ~20 km
437 above the Moho to >30 km below the Moho, dipping north across-strike for ~100 km (Fig. 4, 5 C&D). Both
438 zones of Moho-spanning earthquakes are in locations where receiver-function analyses have been used to argue
439 for eclogitized mafic Indian lower crust in a base-crustal layer (Schulte-Pelkum et al., 2005; Wittlinger et al.,
440 2009, 2004b). Lower-crustal eclogitization in ST is also supported by the difference between Xia et al.'s (2022)
441 receiver function Moho and Zhao et al.'s (2020) gravity Moho, with the gravity Moho up to 15-km deeper (Fig.
442 5C). Because partially eclogitized lower crust has density intermediate between mantle and granulitic lower-
443 crust but wavespeed close to the mantle (Shi et al., 2020; Wittlinger et al., 2009), seismic models may pick the
444 top of eclogite layers as the Moho whereas gravity model may pick the bottom.
445

446 An association between eclogitization processes & intermediate-depth earthquakes has been widely
447 proposed (Austrheim and Boundy, 1994; Jamtveit et al., 2018; Michailos et al., 2021; Shi et al., 2020). Our
448 cross-sections suggest the seismicity continues > 30 km beneath the receiver-function Moho that is interpreted
449 as the base of a continuous Indian lower-crustal layer, into a depth range widely supposed to represent Indian
450 ultramafic upper-mantle. The dipping zones of seismicity therefore likely represent material detaching from the
451 crust & sinking within the mantle, either by delamination (laminar rollback) or dripping (Rayleigh-Taylor
452 instability) (e.g., Beall et al., 2017).
453

454 In west Tibet the intermediate depth seismicity is likely at the northern limit of the underthrust Indian plate
455 (Craig et al., 2012; Wang and Klemperer, 2021), perhaps triggered by impingement of India against the Tarim
456 craton across the Altyn-Tagh Fault (Figs. 4,8). In this location at the north edge of the Indian plate, delamination
457 of a lower-crustal layer (or triggered dripping in the terminology of Beall et al., 2017) (Fig. 8A) is geometrically
458 plausible and potentially induced by the large Moho step across the Altyn-Tagh fault. In contrast, the
459 intermediate-depth seismicity in south Tibet is concentrated ~200 km south of the proposed mantle suture
460 (Klemperer et al., 2022) and ~300 km south of the crustal front (Nábělek et al., 2009) (Fig. 5). In this location
461 it is hard to imagine lower-crust delamination as a sheet (Fig. 8C) being replaced by Indian or Tibet mantle far
462 south of the likely mantle suture, and beneath a remaining eclogite layer interpreted from the continuous receiver-
463 function doublet (Nábělek et al., 2009; Wittlinger et al., 2009). Instead, dripping seems more plausible (Fig. 8D),
464 given the limited cross-strike extent of below-Moho earthquakes (Fig. 5) as well as limited along-strike Moho
465 disruption inferred from seismic images of west-east variability in the receiver-function doublet (Shi et al., 2020).
466 We speculate that dripping at this latitude is triggered by bending of the Indian crust as it underthrusts beneath
467 the High Himalaya and is further localized at this longitude by the NNE-trending Tangra-Yumco and Pumco-
468 Xainza rifts (Shi et al., 2020). The lower crust here is thought from gravity modelling to be only ~30% eclogitized

469 on average, with average density less than the upper mantle (Shi et al., 2020). Rayleigh-Taylor instability
470 requires lower-crustal density to exceed upper-mantle density, achievable locally by geologically instantaneous
471 self-sustaining eclogitization and densification (Malvoisin et al., 2020) following fluid influx along earthquake-
472 generated preferential fluid pathways (Jamtveit et al., 2018) or from autologous fluids of dehydration
473 metamorphism (Hetényi et al., 2007).

474
475 These hypotheses of seismogenic dripping and/or delamination raise the question of whether below-Moho
476 earthquakes in WT & ST are occurring in ultramafic mantle or in eclogitic crust now below the Moho. Tibetan
477 near-Moho earthquakes were first thought to have nucleated in a cold, brittle upper-mantle, leading to the “jelly
478 sandwich” model of crustal rheology (Chen and Molnar, 1983), which was further supported by accumulating
479 discoveries of below-Moho earthquakes (Chen and Yang, 2004) and lower-crustal seismicity gaps (Liang et al.,
480 2008). However, reappraisal of these earthquakes’ depth uncertainties allowed the hypothesis that they were
481 located in the lower crust (Craig et al., 2012; Jackson, 2002; Priestley et al., 2008), leading to the “crème brûlée”
482 model of a strong lower crust above a weaker upper-mantle. The recent demonstration of below-Moho
483 earthquakes existing in both south and northwest Tibet by S_n/L_g methods (Wang and Klemperer, 2021), as well
484 as lower-crustal earthquakes in northwest Tibet (Huang et al., 2011) supported a fully seismogenic lithosphere
485 with earthquakes at all depths. This fully seismogenic behavior may be restricted to the region of below-Moho
486 seismicity beneath the JRS and ATF, and to areas underlain by cratonic Indian lower crust (green in Figs. 4D,
487 5D, 6D). Our areally complete S_n/L_g study across a 20-year time-scale shows that the Tibetan lower crust (cyan
488 in Figs. 4D, 5D, 6D) has almost no ‘better-located’ lower-crustal earthquakes except in the two specific regions
489 of Moho-crossing seismicity. These two regions beneath ST and WT are more seismically active below the
490 Moho than above (Table S6-1), and may correspond to detachment from weak Tibetan middle crust of strong
491 eclogitized Indian lower crust that deforms while sinking into the upper-mantle. The below-Moho earthquakes
492 may be only in crustal lithologies (Klemperer et al., 2013).

493
494 In SE Tibet the geographic pattern of near-Moho earthquakes seems clearly different, and possibly these
495 many events south of the Main Frontal Thrust relates to Himalayan deformation stepping south to the Shillong
496 Plateau, and to complex stresses near the syntaxis where Indian crust subducts both beneath the Himalaya and
497 the Indo-Burman ranges. We defer further discussion of these events pending examination of their S_n/L_g ratios
498 on Indian seismic stations south of the Himalaya.

500 501 **6. Conclusions**

502
503 We have demonstrated a single-station S_n/L_g method to detect below-Moho earthquakes beneath the Tibet
504 plateau, based on synthetics of high-frequency waveforms from the summation of Love modes. We recognize a
505 S_n/L_g amplitude-ratio step increase below the Moho that is largely independent of epicentral distance, crustal
506 thickness, and the existence of a receiver–function doublet. Given the previously demonstrated near-
507 independence of S_n/L_g ratios from focal-mechanism type and receiver azimuth (Wang and Klemperer, 2021),
508 we anticipate the possibility of observing separation of low and high S_n/L_g ratios, and hence distinction of
509 crustal and sub-crustal earthquakes, in many parts of the globe.

510
511 We apply our S_n/L_g method to 595 earthquakes with catalog depths >30 km in Tibet (>20 km in SET) and
512 find with confidence 165 events (excludes events duplicated between $SWT_{(LSA)}$ and $SWT_{(KBL)}$) to have
513 nucleated above Moho and 101 events to have nucleated below Moho, even after taking the uncertainties into
514 consideration (Table S6-2, ‘definitive’ results). Our S_n/L_g results identify concentrated zones of below-Moho
515 earthquakes between the Jinsha River Suture and Altyn-Tagh fault in west Tibet and beneath the transition from
516 High Himalaya to Tethyan Himalaya in south Tibet. The cross-sectional geometry of these earthquake clusters
517 supports an eclogitized Indian lower crust currently delaminating or dripping into the upper mantle in response
518 to local collision and/or bending stresses. The likely existence of these earthquakes in mafic eclogites may allow
519 new constraints on temperatures and strain rates beneath Tibet (Molnar, 2020).

522 **Acknowledgements**

523
524 Shiqi (Axel) Wang provided many helpful suggestions and software assistance.
525
526

527 **References**

- 528
529 Alvizuri, C., Hetényi, G., 2019. Source mechanism of a lower crust earthquake beneath the Himalayas and its
530 possible relation to metamorphism. *Tectonophysics* 769, 128153.
531 <https://doi.org/10.1016/j.tecto.2019.06.023>
- 532 Austrheim, H., Boundy, T.M., 1994. Pseudotachylytes Generated During Seismic Faulting and Eclogitization
533 of the Deep Crust. *Science* 265, 82–83. <https://doi.org/10.1126/science.265.5168.82>
- 534 Baur, J.R., 2007. Seismotectonics of the Himalayas and the Tibetan Plateau : moment tensoranalysis of
535 regional seismograms. Oregon State University.
- 536 Bloch, W., Schurr, B., Yuan, X., Ratschbacher, L., Reuter, S., Kufner, S.-K., Xu, Q., Zhao, J., 2021. Structure
537 and Stress Field of the Lithosphere Between Pamir and Tarim. *Geophys. Res. Lett.* 48,
538 e2021GL095413. <https://doi.org/10.1029/2021GL095413>
- 539 Bondár, I., Engdahl, E.R., Villaseñor, A., Harris, J., Storchak, D., 2015. ISC-GEM: Global Instrumental
540 Earthquake Catalogue (1900–2009), II. Location and seismicity patterns. *Phys. Earth Planet. Inter.*,
541 ISC-GEM Catalogue 239, 2–13. <https://doi.org/10.1016/j.pepi.2014.06.002>
- 542 Bürgmann, R., Dresen, G., 2008. Rheology of the Lower Crust and Upper Mantle: Evidence from Rock
543 Mechanics, Geodesy, and Field Observations. *Annu. Rev. Earth Planet. Sci.* 36, 531–567.
544 <https://doi.org/10.1146/annurev.earth.36.031207.124326>
- 545 Chen, W.-P., Molnar, P., 1983. Focal depths of intracontinental and intraplate earthquakes and their
546 implications for the thermal and mechanical properties of the lithosphere. *J. Geophys. Res. Solid Earth*
547 88, 4183–4214. <https://doi.org/10.1029/JB088iB05p04183>
- 548 Chen, W.-P., Yang, Z., 2004. Earthquakes Beneath the Himalayas and Tibet: Evidence for Strong Lithospheric
549 Mantle. *Science* 304, 1949–1952. <https://doi.org/10.1126/science.1097324>
- 550 Craig, T.J., Copley, A., Jackson, J., 2012. Thermal and tectonic consequences of India underthrusting Tibet.
551 *Earth Planet. Sci. Lett.* 353–354, 231–239. <https://doi.org/10.1016/j.epsl.2012.07.010>
- 552 Craig, T.J., Kelemen, P.B., Hacker, B.R., Copley, A., 2020. Reconciling Geophysical and Petrological
553 Estimates of the Thermal Structure of Southern Tibet. *Geochem. Geophys. Geosystems* 21,
554 e2019GC008837. <https://doi.org/10.1029/2019GC008837>
- 555 Denolle, M.A., Dunham, E.M., Beroza, G.C., 2012. Solving the Surface-Wave Eigenproblem with Chebyshev
556 Spectral Collocation. *Bull. Seismol. Soc. Am.* 102, 1214–1223. <https://doi.org/10.1785/0120110183>
- 557 Diehl, T., Singer, J., Hetényi, G., Grujic, D., Clinton, J., Giardini, D., Kissling, E., 2017. Seismotectonics of
558 Bhutan: Evidence for segmentation of the Eastern Himalayas and link to foreland deformation. *Earth
559 Planet. Sci. Lett.* 471, 54–64. <https://doi.org/10.1016/j.epsl.2017.04.038>
- 560 Dziewonski, A.M., Chou, T.-A., Woodhouse, J.H., 1981. Determination of earthquake source parameters from
561 waveform data for studies of global and regional seismicity. *J. Geophys. Res. Solid Earth* 86, 2825–
562 2852. <https://doi.org/10.1029/JB086iB04p02825>
- 563 Fan, G.-W., Lay, T., 2003. Strong Lg wave attenuation in the Northern and Eastern Tibetan Plateau measured
564 by a two-station/two-event stacking method. *Geophys. Res. Lett.* 30.
565 <https://doi.org/10.1029/2002GL016211>
- 566 Gao, R., Lu, Z., Klempner, S.L., Wang, H., Dong, S., Li, W., Li, H., 2016. Crustal-scale duplexing beneath
567 the Yarlung Zangbo suture in the western Himalaya. *Nat. Geosci.* 9, 555–560.
568 <https://doi.org/10.1038/ngeo2730>
- 569 Grujic, D., Warren, C.J., Wooden, J.L., 2011. Rapid synconvergent exhumation of Miocene-aged lower
570 orogenic crust in the eastern Himalaya. *Lithosphere* 3, 346–366. <https://doi.org/10.1130/L154.1>
- 571 Henry, P., Le Pichon, X., Goffé, B., 1997. Kinematic, thermal and petrological model of the Himalayas:
572 constraints related to metamorphism within the underthrust indian crust and topographic elevation.
573 *Tectonophysics, Collisional Orogens: Zones of Active Transfer Between Crust and Mantle* 273, 31–
574 56. [https://doi.org/10.1016/S0040-1951\(96\)00287-9](https://doi.org/10.1016/S0040-1951(96)00287-9)

575 Hetényi, G., Cattin, R., Brunet, F., Bollinger, L., Vergne, J., Nábělek, J.L., Diament, M., 2007. Density
576 distribution of the India plate beneath the Tibetan plateau: Geophysical and petrological constraints on
577 the kinetics of lower-crustal eclogitization. *Earth Planet. Sci. Lett.* 264, 226–244.
578 <https://doi.org/10.1016/j.epsl.2007.09.036>

579 Huang, G.-C.D., Roecker, S.W., Levin, V., 2011. Lower-crustal earthquakes in the West Kunlun range.
580 *Geophys. Res. Lett.* 38. <https://doi.org/10.1029/2010GL045893>

581 Jackson, J., 2002. Strength of the continental lithosphere: Time to abandon the jelly sandwich? *GSA Today* 12,
582 4. [https://doi.org/10.1130/1052-5173\(2002\)012<0004:SOTCLT>2.0.CO;2](https://doi.org/10.1130/1052-5173(2002)012<0004:SOTCLT>2.0.CO;2)

583 Jamtveit, B., Ben-Zion, Y., Renard, F., Austrheim, H., 2018. Earthquake-induced transformation of the lower
584 crust. *Nature* 556, 487–491. <https://doi.org/10.1038/s41586-018-0045-y>

585 Jiang M., Zhou S., Tong X., Liang X., Chen Y., 2009. Accurate depth determination of deep earthquake in
586 southern Tibet and its geodynamic implication. *Chin. J. Geophys.* 52, 2237–2244.
587 <https://doi.org/10.3969/j.issn.0001-5733.2009.09.007>

588 Kennett, B.L.N., 1986. Lg waves and structural boundaries. *Bull. Seismol. Soc. Am.* 76, 1133–1141.
589 <https://doi.org/10.1785/BSSA0760041133>

590 Kind, R., Yuan, X., Saul, J., Nelson, D., Sobolev, S.V., Mechie, J., Zhao, W., Kosarev, G., Ni, J., Achauer, U.,
591 Jiang, M., 2002. Seismic Images of Crust and Upper Mantle Beneath Tibet: Evidence for Eurasian
592 Plate Subduction. *Science* 298, 1219–1221. <https://doi.org/10.1126/science.1078115>

593 Klemperer, S.L., Kennedy, B.M., Sastry, S.R., Makovsky, Y., Harinarayana, T., Leech, M.L., 2013. Mantle
594 fluids in the Karakoram fault: Helium isotope evidence. *Earth Planet. Sci. Lett.* 366, 59–70.
595 <https://doi.org/10.1016/j.epsl.2013.01.013>

596 Klemperer, S.L., Zhao, P., Whyte, C.J., Darrah, T.H., Crossey, L.J., Karlstrom, K.E., Liu, T., Winn, C., Hilton,
597 D.R., Ding, L., 2022. Limited underthrusting of India below Tibet: $^3\text{He}/^4\text{He}$ analysis of thermal
598 springs locates the mantle suture in continental collision. *Proc. Natl. Acad. Sci.* 119, e2113877119.
599 <https://doi.org/10.1073/pnas.2113877119>

600 Knopoff, L., Schwab, F., Kauselt, E., 1973. Interpretation of Lg*. *Geophys. J. Int.* 33, 389–404.
601 <https://doi.org/10.1111/j.1365-246X.1973.tb02375.x>

602 Kufner, S.-K., Schurr, B., Sippl, C., Yuan, X., Ratschbacher, L., Akbar, A. s/of M., Ischuk, A., Murodkulov,
603 S., Schneider, F., Mechie, J., Tilmann, F., 2016. Deep India meets deep Asia: Lithospheric
604 indentation, delamination and break-off under Pamir and Hindu Kush (Central Asia). *Earth Planet.*
605 *Sci. Lett.* 435, 171–184. <https://doi.org/10.1016/j.epsl.2015.11.046>

606 Levin, V., Huang, G.D., Roecker, S., 2013. Crust–mantle coupling at the northern edge of the Tibetan plateau:
607 Evidence from focal mechanisms and observations of seismic anisotropy. *Tectonophysics, Active*
608 *Tectonic Deformation of the Tibetan Plateau and Great Earthquakes* 584, 221–229.
609 <https://doi.org/10.1016/j.tecto.2012.05.013>

610 Liang, X., Zhou, S., Chen, Y.J., Jin, G., Xiao, L., Liu, P., Fu, Y., Tang, Y., Lou, X., Ning, J., 2008. Earthquake
611 distribution in southern Tibet and its tectonic implications. *J. Geophys. Res. Solid Earth* 113.
612 <https://doi.org/10.1029/2007JB005101>

613 Maggi, A., Jackson, J.A., McKenzie, D., Priestley, K., 2000. Earthquake focal depths, effective elastic
614 thickness, and the strength of the continental lithosphere. *Geology* 28, 495–498.
615 [https://doi.org/10.1130/0091-7613\(2000\)28<495:EFDEET>2.0.CO;2](https://doi.org/10.1130/0091-7613(2000)28<495:EFDEET>2.0.CO;2)

616 Malvoisin, B., Zhang, C., Müntener, O., Baumgartner, L.P., Kelemen, P.B., Party, O.D.P.S., 2020.
617 Measurement of Volume Change and Mass Transfer During Serpentinization: Insights From the
618 Oman Drilling Project. *J. Geophys. Res. Solid Earth* 125, e2019JB018877.
619 <https://doi.org/10.1029/2019JB018877>

620 McNamara, D.E., Owens, T.J., Walter, W.R., 1995. Observations of regional phase propagation across the
621 Tibetan Plateau. *J. Geophys. Res. Solid Earth* 100, 22215–22229. <https://doi.org/10.1029/95JB01863>

622 Michailos, K., Carpenter, N.S., Hetényi, G., 2021. Spatio-Temporal Evolution of Intermediate-Depth
623 Seismicity Beneath the Himalayas: Implications for Metamorphism and Tectonics. *Front. Earth Sci.* 9.

624 Mitra, S., Priestley, K.F., Borah, K., Gaur, V.K., 2018. Crustal Structure and Evolution of the Eastern
625 Himalayan Plate Boundary System, Northeast India. *J. Geophys. Res. Solid Earth* 123, 621–640.
626 <https://doi.org/10.1002/2017JB014714>

- 627 Molnar, P., 2020. The Brittle-Plastic Transition, Earthquakes, Temperatures, and Strain Rates. *J. Geophys.*
628 *Res. Solid Earth* 125, e2019JB019335. <https://doi.org/10.1029/2019JB019335>
- 629 Monsalve, G., McGovern, P., Sheehan, A., 2009. Mantle fault zones beneath the Himalayan collision: Flexure
630 of the continental lithosphere. *Tectonophysics, Continental Collision, Partial Melting and Ductile*
631 *Deformation in The Tibetan-Himalayan Orogenic Belt* 477, 66–76.
632 <https://doi.org/10.1016/j.tecto.2008.12.014>
- 633 Monsalve, G., Sheehan, A., Schulte-Pelkum, V., Rajaure, S., Pandey, M.R., Wu, F., 2006. Seismicity and one-
634 dimensional velocity structure of the Himalayan collision zone: Earthquakes in the crust and upper
635 mantle. *J. Geophys. Res. Solid Earth* 111. <https://doi.org/10.1029/2005JB004062>
- 636 Mousavi, S.M., Cramer, C.H., Langston, C.A., 2014. Average QLg, QSn, and observation of Lg blockage in
637 the Continental Margin of Nova Scotia. *J. Geophys. Res. Solid Earth* 119, 7722–7744.
638 <https://doi.org/10.1002/2014JB011237>
- 639 Nábělek, J., Hetényi, G., Vergne, J., Sapkota, S., Kafle, B., Jiang, M., Su, H., Chen, J., Huang, B.-S., Team,
640 the H.-C., 2009. Underplating in the Himalaya-Tibet Collision Zone Revealed by the Hi-CLIMB
641 Experiment. *Science* 325, 1371–1374. <https://doi.org/10.1126/science.1167719>
- 642 Parija, M.P., Kumar, S., Tiwari, V.M., Rao, N.P., Kumar, N., Biswal, S., Singh, I., 2018. Microseismicity,
643 tectonics and seismic potential in the Western Himalayan segment, NW Himalaya, India. *J. Asian*
644 *Earth Sci.* 159, 1–16. <https://doi.org/10.1016/j.jseae.2018.03.016>
- 645 PDE, 2022. The Preliminary Determination of Epicenters (PDE) Bulletin [WWW Document]. URL
646 <https://earthquake.usgs.gov/data/comcat/catalog/us/> (accessed 8.9.22).
- 647 Press, F., Ewing, M., 1952. Two slow surface waves across North America*. *Bull. Seismol. Soc. Am.* 42, 219–
648 228. <https://doi.org/10.1785/BSSA0420030219>
- 649 Priestley, K., Jackson, J., McKenzie, D., 2008. Lithospheric structure and deep earthquakes beneath India, the
650 Himalaya and southern Tibet. *Geophys. J. Int.* 172, 345–362. <https://doi.org/10.1111/j.1365-246X.2007.03636.x>
- 651 Schulte-Pelkum, V., Monsalve, G., Sheehan, A., Pandey, M.R., Sapkota, S., Bilham, R., Wu, F., 2005.
652 Imaging the Indian subcontinent beneath the Himalaya. *Nature* 435, 1222–1225.
653 <https://doi.org/10.1038/nature03678>
- 654 Schulte-Pelkum, V., Monsalve, G., Sheehan, A.F., Shearer, P., Wu, F., Rajaure, S., 2019. Mantle earthquakes
655 in the Himalayan collision zone. *Geology* 47, 815–819. <https://doi.org/10.1130/G46378.1>
- 656 Shi, D., Klemperer, S.L., Shi, J., Wu, Z., Zhao, W., 2020. Localized foundering of Indian lower crust in the
657 India–Tibet collision zone. *Proc. Natl. Acad. Sci.* 117, 24742–24747.
658 <https://doi.org/10.1073/pnas.2000015117>
- 659 Shi, F., Wang, Y., Yu, T., Zhu, L., Zhang, J., Wen, J., Gasc, J., Incel, S., Schubnel, A., Li, Z., Chen, T., Liu,
660 W., Prakapenka, V., Jin, Z., 2018. Lower-crustal earthquakes in southern Tibet are linked to
661 eclogitization of dry metastable granulite. *Nat. Commun.* 9, 3483. <https://doi.org/10.1038/s41467-018-05964-1>
- 662 Stephens, C., Isacks, B.L., 1977. Toward an understanding of Sn: Normal modes of love waves in an oceanic
663 structure. *Bull. Seismol. Soc. Am.* 67, 69–78. <https://doi.org/10.1785/BSSA0670010069>
- 664 Taylor, M., Yin, A., 2009. Active structures of the Himalayan-Tibetan orogen and their relationships to
665 earthquake distribution, contemporary strain field, and Cenozoic volcanism. *Geosphere* 5, 199–214.
666 <https://doi.org/10.1130/GES00217.1>
- 667 Wang, S., Klemperer, S.L., 2021. Love-wave normal modes discriminate between upper-mantle and crustal
668 earthquakes: Simulation and demonstration in Tibet. *Earth Planet. Sci. Lett.* 571, 117089.
669 <https://doi.org/10.1016/j.epsl.2021.117089>
- 670 Wittlinger, G., Farra, V., Hetényi, G., Vergne, J., Nábělek, J., 2009. Seismic velocities in Southern Tibet lower
671 crust: a receiver function approach for eclogite detection. *Geophys. J. Int.* 177, 1037–1049.
672 <https://doi.org/10.1111/j.1365-246X.2008.04084.x>
- 673 Wittlinger, G., Farra, V., Vergne, J., 2004a. Lithospheric and upper mantle stratifications beneath Tibet: New
674 insights from Sp conversions. *Geophys. Res. Lett.* 31. <https://doi.org/10.1029/2004GL020955>
- 675 Wittlinger, G., Vergne, J., Tapponnier, P., Farra, V., Poupinet, G., Jiang, M., Su, H., Herquel, G., Paul, A.,
676 2004b. Teleseismic imaging of subducting lithosphere and Moho offsets beneath western Tibet. *Earth*
677 *Planet. Sci. Lett.* 221, 117–130. [https://doi.org/10.1016/S0012-821X\(03\)00723-4](https://doi.org/10.1016/S0012-821X(03)00723-4)

680 Xia, B., Artemieva, I., Thybo, H., Klemperer, S., 2022. Regional variability in the thermal structure of Tibetan
681 Lithosphere (No. EGU22-7161). Presented at the EGU22, Copernicus Meetings.
682 <https://doi.org/10.5194/egusphere-egu22-7161>

683 Yang, X., Lay, T., Xie, X.-B., Thorne, M.S., 2007. Geometric Spreading of Pn and Sn in a Spherical Earth
684 Model. *Bull. Seismol. Soc. Am.* 97, 2053–2065. <https://doi.org/10.1785/0120070031>

685 Zhang, Z., Wang, Y., Houseman, G.A., Xu, T., Wu, Z., Yuan, X., Chen, Y., Tian, X., Bai, Z., Teng, J., 2014.
686 The Moho beneath western Tibet: Shear zones and eclogitization in the lower crust. *Earth Planet. Sci.*
687 *Lett.* 408, 370–377. <https://doi.org/10.1016/j.epsl.2014.10.022>

688 Zhao, G., Liu, J., Chen, B., Kaban, Mikhail.K., Zheng, X., 2020. Moho Beneath Tibet Based on a Joint
689 Analysis of Gravity and Seismic Data. *Geochem. Geophys. Geosystems* 21, e2019GC008849.
690 <https://doi.org/10.1029/2019GC008849>

691 Zhao, L.-S., Helmberger, D.V., Harkrider, D.G., 1991. Shear-velocity structure of the crust and upper mantle
692 beneath the Tibetan Plateau and southeastern China. *Geophys. J. Int.* 105, 713–730.
693 <https://doi.org/10.1111/j.1365-246X.1991.tb00807.x>

694 Zhu, L., Helmberger, D.V., 1996. Intermediate depth earthquakes beneath the India-Tibet Collision Zone.
695 *Geophys. Res. Lett.* 23, 435–438. <https://doi.org/10.1029/96GL00385>

696
697

Supplementary Materials for:

Numerous Tibetan lower-crustal and upper-mantle earthquakes detected by Sn/Lg ratios suggest crustal delamination or drip tectonics

Xiaohan Song, Simon L. Klemperer

Department of Geophysics, Stanford University, Stanford, CA 94305, USA

Sections

S1. Definition of Sn and Lg windows for synthetics & data

S2. Flattened velocity model

S3. Catalog selection

S4. The calculation of Sn/Lg and ln(Sn/Lg) and their uncertainties

S5. Geometric spreading detrend

S6. Earthquake classifications

S7. Sn and Lg Blockage or Leakage

S8. Filter applied to the Moho map

S9. Comparison between LSA and KBL in west Tibet

S10. Sn/Lg results from the Qiangtang

Tables Attached Separately

Table SA. Source parameters and waveforms of WT earthquakes, and their Sn/Lg ratios

Table SB. Source parameters and waveforms of ST earthquakes, and their Sn/Lg ratios

Table SC. Source parameters and waveforms of SET earthquakes, and their Sn/Lg ratios

S1. Definition of Sn and Lg windows for synthetics & data

The picking of Sn and Lg phases is based on ray tracing in a simple 1-D model with uniform crust and mantle and depends only on epicentral distance. We set the Sn onset time, T_{Sn} , to be the S head-wave arrival (Sn) for crustal earthquakes and the direct S arrival (Sg) for mantle earthquakes. The Lg onset time, T_{Lg} , is set to be the direct S arrival (Sg) for crustal earthquakes, and Lg from a sub-Moho earthquake is treated as direct S from the Moho vertically above the earthquake (Fig. S1-1). T_{Sn} and T_{Lg} can be calculated through the following equations in which R is the epicentral distance, d is the source depth, H is the Moho depth, and v_{sc} & v_{sm} are crustal & mantle shear wavespeeds:

$$T_{Lg} = \frac{\sqrt{R^2 + d^2}}{v_{sc}} \quad \text{Lg arrival for crustal earthquakes (S1.1a)}$$

$$T_{Lg} = \frac{\sqrt{R^2 + H^2}}{v_{sc}} + \frac{d - H}{v_{sm}} \quad \text{Lg arrival for mantle earthquakes (S1.1b)}$$

$$T_{Sn} = \frac{R}{v_{sm}} + (2H - d) * \frac{\sqrt{v_{sm}^2 - v_{sc}^2}}{v_{sm}v_{sc}} \quad \text{Sn arrival for crustal earthquakes (S1.1c)}$$

$$T_{Sn} = \frac{\sqrt{x^2 + (d - H)^2}}{v_{sm}} + \frac{\sqrt{(R - x)^2 + H^2}}{v_{sc}} \quad \text{Sn arrival for mantle earthquakes (S1.1d)}$$

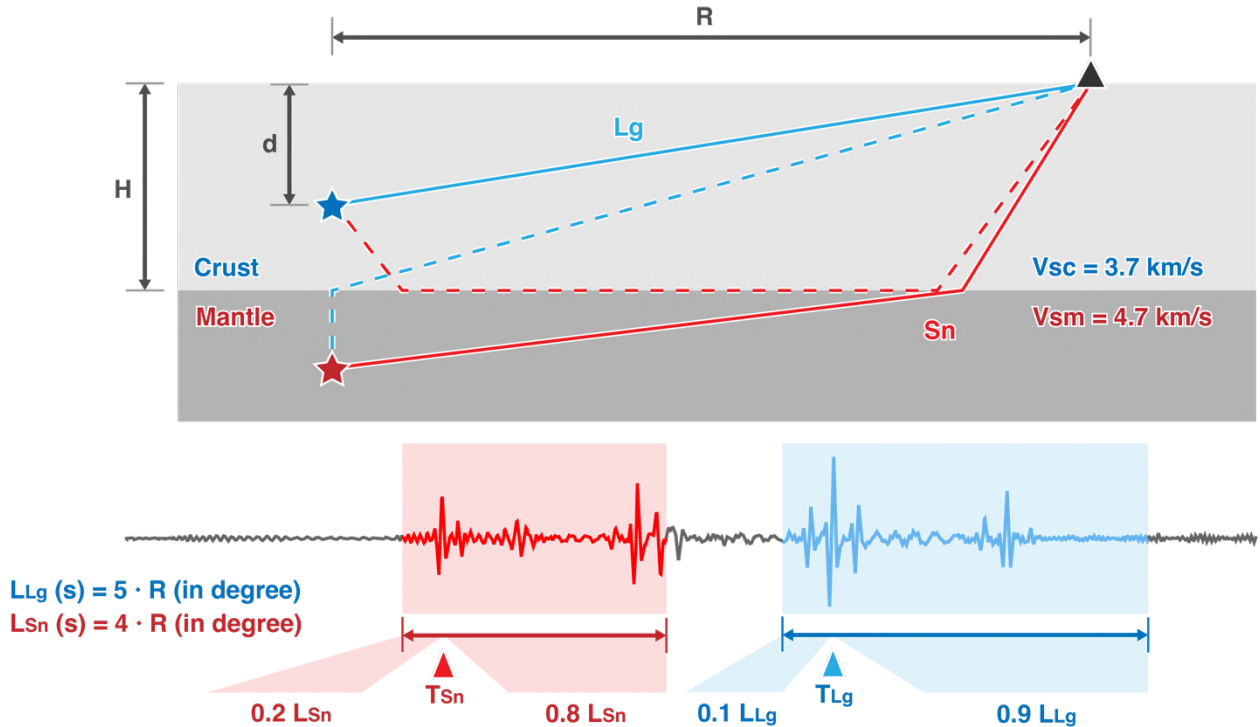
where x is the solution of:

$$\frac{x}{v_{sm}\sqrt{x^2 + (d - H)^2}} = \frac{R - x}{v_{sc}\sqrt{(R - x)^2 + H^2}} \quad (\text{S1.2})$$

For our synthetics, d , H , and R are fixed and known, as is the velocity structure (v_{sc} , v_{sm}). For the real data, d is set at the catalog depth; H is set at 70 km; and R is sufficiently well-known. Crustal and mantle wavespeed are defined as $v_{sc} = 3.7$ km/s and $v_{sm} = 4.7$ km/s.

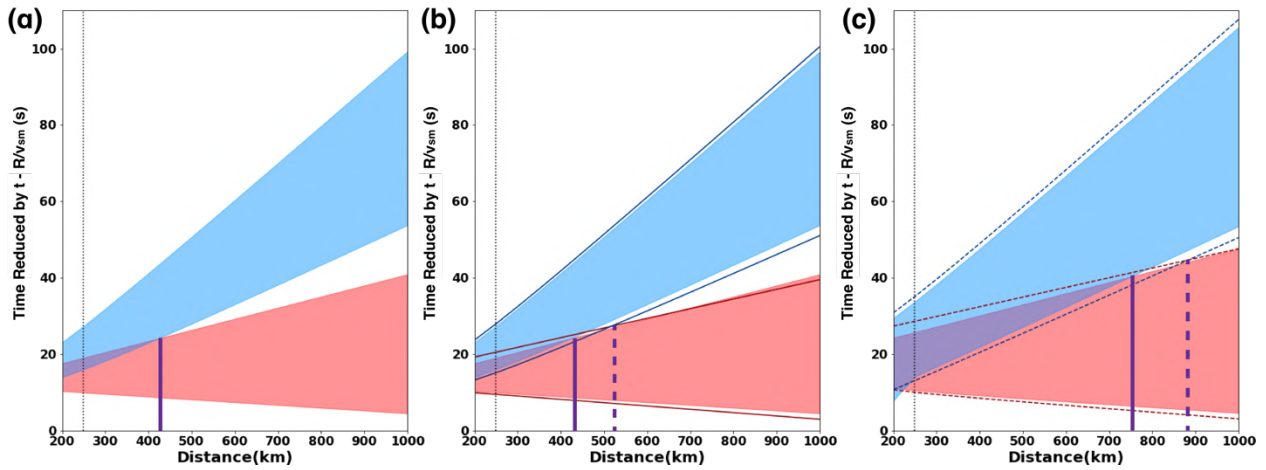
The windows in which we pick the Sn and Lg amplitudes, L_{Sn} and L_{Lg} , have lengths set to be 4 and 5 times of the source-receiver distance in degrees, respectively. The Sn window begins at $T_{Sn} - 0.2L_{Sn}$, and the Lg window begins at $T_{Lg} - 0.1L_{Lg}$. When the two windows overlap at short offsets, the Sn window is truncated at $T_{Lg} - 0.05L_{Lg}$ and the Lg window starts at this time. Our method differs slightly from some previous studies that use maximum and minimum mantle and crustal velocities (“velocity-range” method) to determine the start and end of the Sn and Lg windows (Mousavi et al., 2014; Wang and Klemperer, 2021). Our method (Fig. S1-2a) is almost equivalent to the velocity-range method if v_{sm} is in the range 4.2–4.9 km/s and v_{sc} 3.2–3.8 km/s (Fig. S1-2b) and our windows are very comparable to those used by Wang and Klemperer (2021) who used v_{sm} from 4.3–4.8 km/s and v_{sc} from 3.1–3.6 km/s. We prefer our window-determination method because we include a few seconds of the waveform before the predicted earliest arrivals to more-certainly capture the phase onset, and because we only require two parameters, average v_{sm} and v_{sc} , instead of four (max & min v_{sc} and v_{sm}).

We select 250 km to be the minimum distance for our Sn/Lg analysis, beyond which a significant fraction of the Sn and Lg windows should not overlap, even though some overlap remains out to $R \sim 400$ –500 km.



69
70
71
72

Fig. S1-1. Ray paths used to calculate the windows in which Sn and Lg phases arrive.



73
74

Fig. S1-2. Window ranges for Sn and Lg phases (reduced travel-time vs. offset). (a) Windows determined as in Fig. S1-1 with fixed source depth 70 km. Red: Sn window. Blue: Lg window. (b) as (a), with addition of lines representing windows determined by velocity-range methods (v_{sm} : 4.2–4.9 km/s; v_{sc} : 3.2–3.8 km/s) with fixed source depth 70 km. (c) Window ranges determined for source depths 30–100 km. Solid and dashed lines: window ranges determined with our method and velocity range method, respectively. In all three parts, vertical dotted line marks the 250-km cut-off distance below which we do not attempt to measure Sn/Lg ratios, and solid and dashed vertical lines mark the distance beyond which the Sn and Lg windows no longer overlap under different scenarios.

82

To test the sensitivity of measured Sn/Lg to uncertainties in H , d , v_{sc} , v_{sm} , etc., we use our synthetics for our 70-km single-layer crust (Fig. 3A) and re-calculate Sn and Lg windows and resultant Sn/Lg amplitude ratio for different values of earthquake depth d , Moho depth H , crustal wavespeed v_{sc} and mantle wavespeed v_{sm} (Fig. S1-3).

87

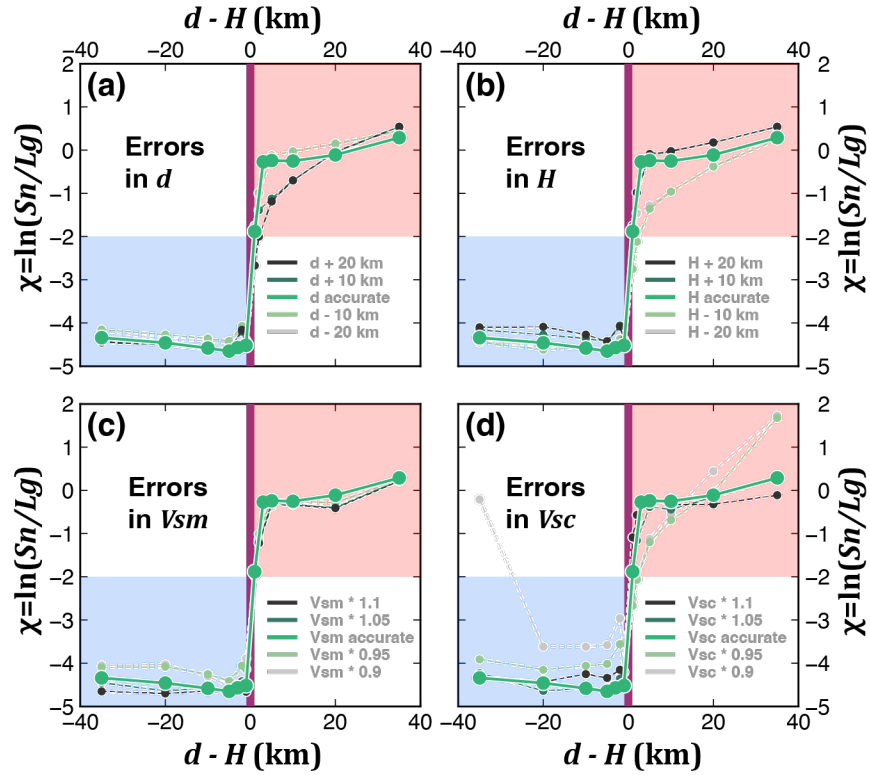


Fig. S1-3. Effect of uncertainties in d , H , v_{sm} , and v_{sc} on $\ln(Sn/Lg)$.

A 20-km variation of H and d ($> 25\%$) has limited influence on the Sn/Lg vs $d - H$ plots, meaning that our Sn/Lg method is robust to uncertain Moho and source depths (Fig. S1-3 a, b). A 10% uncertainty in the mantle S wavespeed is similarly unimportant (Fig. S1-3 c). However, 10% uncertainty in average crustal shear wavespeed can potentially have a dramatic effect on Sn/Lg (Fig. S1-3 d) if a lower-than-expected v_{sc} delays Lg arrivals beyond the Lg window so artificially increases the measured Sn/Lg . Fortunately, Sn and Lg in Tibet are well characterized with onset velocities of 4.6 and 3.6 km/s at regional distances (McNamara et al., 1995a) and our Lg windows capture all arrivals down to $v_{sc} = 3.2$ km/s.

For the phase picking model applied in our main study, we set the Moho depth H to be 70 km, the mantle S -wave velocity $v_{sm} = 4.7$ km/s, and the crustal S -wave velocity $v_{sc} = 3.7$ km/s. Even a 5% reduction in regional wavespeeds ($v_{sm} \leq 4.5$ km/s; $v_{sc} \leq 3.5$ km/s) or 5% increase ($v_{sm} \geq 4.9$ km/s; $v_{sc} \geq 3.9$ km/s) seems quite unlikely (McNamara et al., 1995a).

S2. Flattened velocity model

The input model for our GESC synthetics is the simplified Tibetan velocity model of Zhao et al. (1991). Because GESC expects a flattened earth model, here we show the implied spherical-Earth velocity & density model calculated from the flattened input model (Fig. S2). Velocity differences caused by the flattening transform are $< 6\%$, within the tolerance of our Sn/Lg method.

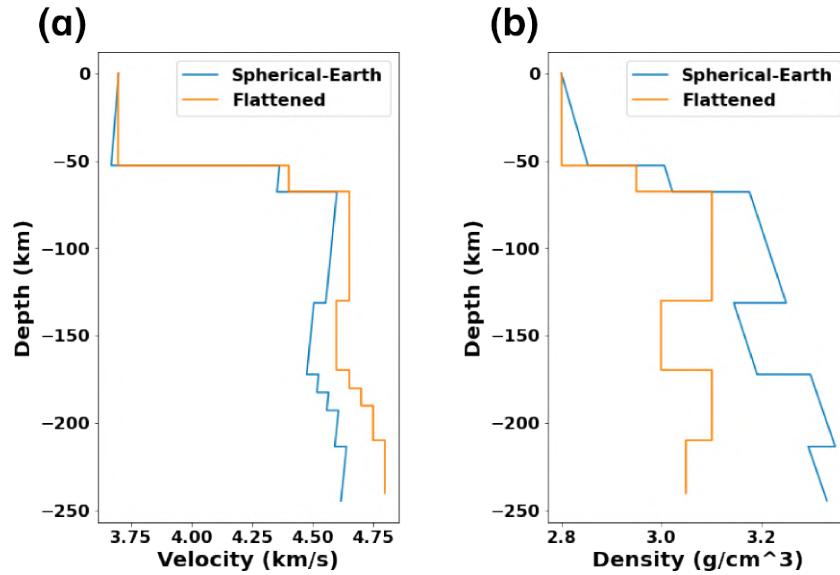


Fig. S2. Comparison between the flattened and spherical-Earth velocity (a) & density (b) model.

S3. Catalog selection

We use histograms of the depth distribution of earthquakes to check there is no temporal bias of the USGS-NEIC PDE locations (Fig. S3-1). Aside from the peaks in the USGS-NEIC histograms representing earthquakes arbitrarily assigned to 10 km, 33 km, or 35 km, the histogram for 1999-2007 (after LSA data become available) (Fig. S3-1b) and 2008-2021 (after KBL provided data) (Fig. S3-1c) have similar features. Most earthquakes locate above 60 km and only very few are deeper. In contrast, the histogram for 1991-1998 (which we did not use as neither LSA nor KBL was operational) (Fig. S3-1a) has a more uniform distribution with depth, likely indicative of larger depth errors because of the paucity of stations at that time.

We also compare the USGS histograms in our south Tibet (ST) with regional catalogs from previous studies in this area (Jiang et al., 2009; Michailos et al., 2021; Monsalve et al., 2006). All four catalogs show an earthquake cluster around 70 km depth. Considering the variability between the three relocation catalogs that have smaller and different timescales, the difference between the USGS histogram and the other three seems unimportant.

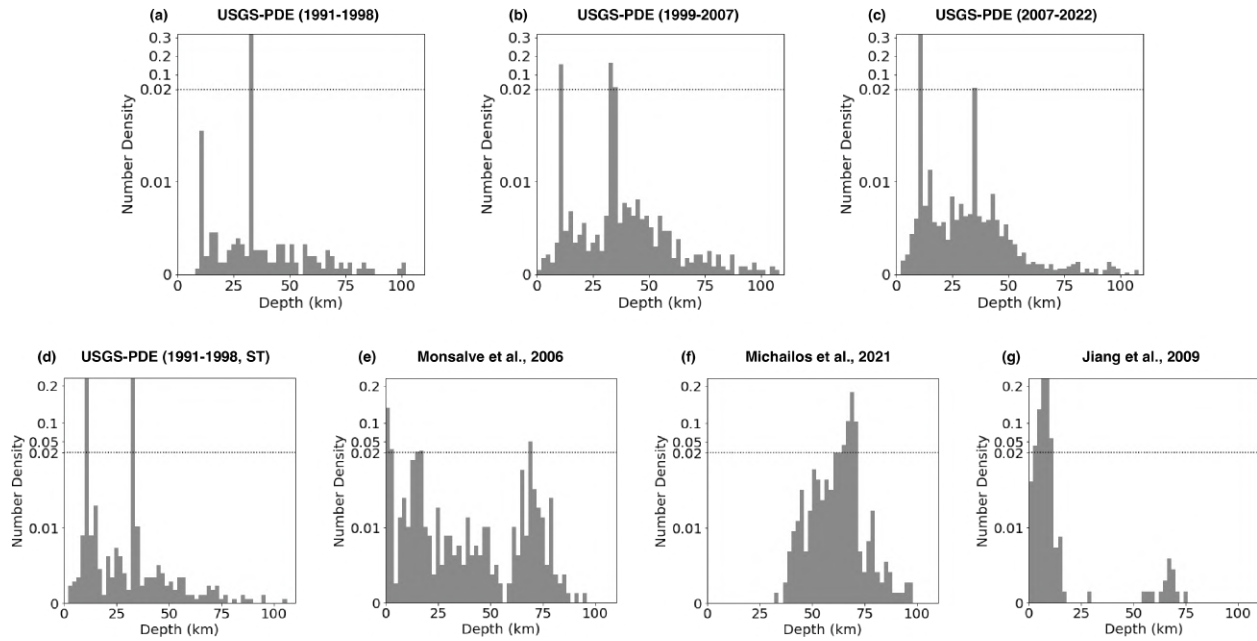


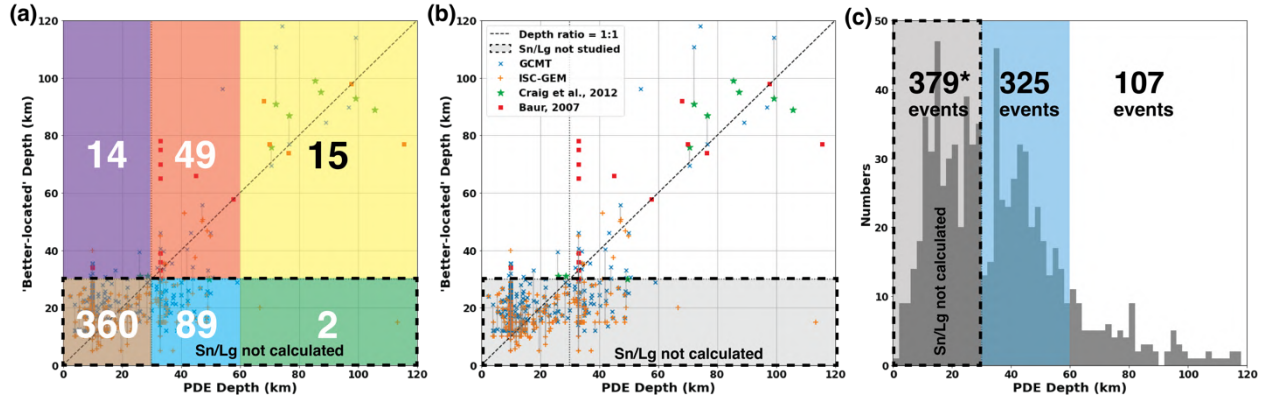
Fig. S3-1. (a - c). Histograms of the earthquake depths in USGS-PDE catalogs for three different epochs. (d - g). Histograms for earthquake depths for South Tibet only in four different catalogs. Note scale change in ordinate (number density) at 0.02. Note the catalog of Michailos et al. (2021) only includes events with initial depth determinations > 40 km.

We compared USGS-PDE catalog depths and the ISC-GEM, GCMT, Craig et al. (2012) and Baur (2007) catalog depths across our entire Tibet study region to help evaluate depth uncertainty (Fig. S3-2). 155 events with PDE depths ≥ 30 km also appear in one of these other four catalogs (for simplicity here we ignore additional compilations (Alvizuri and Hetényi, 2019; Bloch et al., 2021; Diehl et al., 2017; Michailos et al., 2021; Monsalve et al., 2006; Parija et al., 2018) are limited in time and space and have very few overlapping earthquakes). Of 374 events with PDE depths <30 km, 14 (< 5%) are likely deeper, but none have published locations >40 km. Of 138 events with PDE depths from 30 to 60 km, only 49 (~one-third) are confirmed as deep (>30 km) events by another catalog; but of the 17 events with PDE depths >60 km 15 (~90%) also have hypocentral depths >60 km in at least one of the four nominally more accurate catalogs (Fig. S3-2a).

Fig. S3-2b shows that individual events can have very large discrepancies between catalogs. The three PDE events with depths from 55–60 km appear respectively 40-km deeper in the GCMT catalog, at the same depth in Baur (2007) and 30-km shallower in GCMT. But our ‘better-located’ catalogs also have significant uncertainty: two events with PDE depths ~70–80 km have GCMT depths ~10-km shallower than the Craig et al. (2012) re-location, and a third has a GCMT depth ~25-km deeper than in Craig et al. (2012).

These results inform the likelihood that we have missed additional deep earthquakes, or calculated S_n/L_g ratios for shallow events <30 km, when working with PDE events not reported elsewhere. We did not calculate S_n/L_g ratios for the 379 PDE events not sufficiently well-recorded to appear in other catalogs that have depths <30 km (but excluding those with depths fixed at 10.0 km which we expect to have the largest uncertainty) (Fig. S3-2c). We may thereby have missed ~15 events with true depths >30 km, but likely no events below 60 km, based on the 374 PDE earthquakes above 30 km for which we also have ‘better locations’ (Fig. S3-2a). 325 PDE events in the range 30–60 km but not reported elsewhere passed our S_n/L_g SNR test, and are included in our catalog, even though Fig. S3-2a suggests that ~ 200 of these have true depths < 30 km. A handful of these 325 events also likely have true depths >70 km (2 of 138 in this depth range were re-categorized to >70 km in Fig. S3-2a,b), so potentially are mantle events that, if correctly determined as such by our S_n/L_g method, would be recorded as failures of our method (Supplementary Material S6). Of 107 PDE events with depths >60 km, not reported

169 elsewhere but that passed our Sn/Lg SNR test, a dozen are likely upper-crustal events, and again if correctly
 170 determined as such by our Sn/Lg method would be recorded as failures of our method (Supplementary Material
 171 S6).
 172



173
 174
 175 **Fig. S3-2. (a) Depth comparison between the USGS PDE catalog and the ISC-GEM, GCMT, Baur (2007) and**
 176 **Craig et al. (2012) locations, showing number of events in different parts of the plot. (b) Same plot with no overlay.**
 177 Vertical lines link same event in two different 'better-located' catalogs. Shaded region marks the events not included
 178 in our Sn/Lg analysis. (c) Depths of PDE earthquakes that do not appear in any other catalog. Above 30 km this
 179 excludes all events with depth fixed at 10.0 km; below 30 km we exclude earthquakes with assigned 33 km or 35 km
 180 depths that lack uncertainties, and only include events which passed our Sn/Lg SNR threshold.
 181

182 Our primary catalog includes all $m \geq 3.5$ earthquakes with $d \geq 30$ km from 1998-2021 from the PDE catalog.
 183 We first delete those earthquakes 33 km or 35 km deep for which no uncertainties were given. We also search
 184 all other catalogs which likely have better depth locations, including ISC-GEM, GCMT, and previous relocation
 185 & focal-mechanism studies, selecting all $m \geq 3.2$ earthquakes. Duplicate earthquakes are removed, and a single
 186 catalog depth assigned to each event duplicated in multiple non-USGS catalogs, prioritizing the relocation study
 187 with the smallest quoted uncertainty, then GCMT locations, and then ISC locations. All these better-located
 188 earthquakes are marked with stars on figures in the main text.
 189

190
 191
 192 **S4. Calculation of Sn/Lg and $\ln(Sn/Lg)$ and their uncertainties**
 193

194 We measure the root mean square (RMS) amplitudes, A_{Sn} and A_{Lg} , of the Sn and Lg -windows. We measure the
 195 noise in a window from 30–15 s before the calculated first P arrival. We measure the signal-to-noise ratio (SNR)
 196 for both windows ($SNR_{Lg} = A_{Lg}/A_{noise}$; $SNR_{Sn} = A_{Sn}/A_{noise}$) and discard all earthquakes for which both
 197 $SNR_{Lg} < 3$ and $SNR_{Sn} < 3$. For the remaining earthquakes we calculate the Sn/Lg ratio as uncertainties of the
 198 Sn and Lg amplitudes, σ_{Sn} and σ_{Lg} . Finally, we calculate the uncertainties in Sn/Lg and $\ln(Sn/Lg)$.
 199

$$Sn/Lg = \frac{A_{Sn}}{A_{Lg}} \quad (S4.1)$$

$$\sigma_{Sn/Lg} = \sqrt{\frac{\sigma_{Sn}^2}{A_{Lg}^2} + \frac{A_{Sn}^2 \sigma_{Lg}^2}{(A_{Lg}^2)^2}} \quad (S4.2)$$

$$\sigma_{\ln(Sn/Lg)} = \frac{\sigma_{Sn/Lg}}{Sn/Lg} \quad (S4.3)$$

200
 201 An important note is that this uncertainty estimation only takes into consideration random noise. Our
 202 observations (Table S1) and as shown by Wang and Klemperer's (2021, their Fig. S9) real seismograms, the

203 influence of SH -converted P wave can be non-negligible. We lack a simple method to account for this high-
 204 frequency Rayleigh-Love coupling.

205

206 Beside calculating the Sn/Lg amplitude ratios with window RMS amplitudes, we also test using the peak
 207 amplitudes:

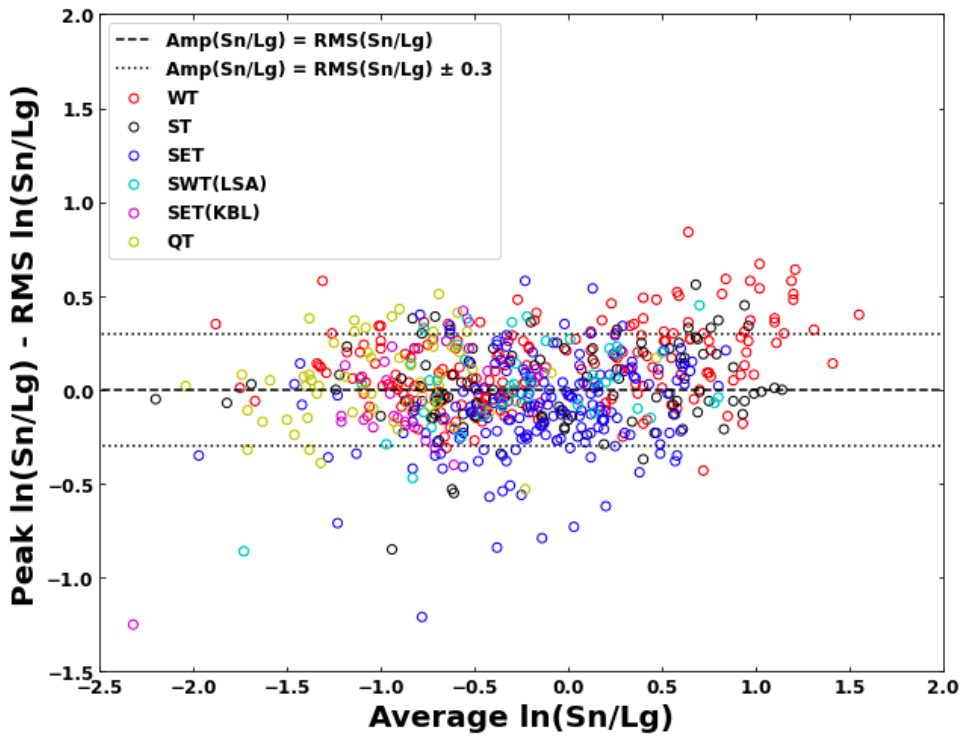
208

$$Sn/Lg = \frac{\max\{|Sn|\}}{\max\{|Lg|\}} \quad (S4.4)$$

209

210 Comparing the Sn/Lg amplitude ratios and the Sn/Lg RMS ratios (Fig. S4) for all the seismograms we have
 211 used for Sn/Lg calculation in this study, we find the difference between these two types of ratios (natural log
 212 value) is typically $< \pm 0.3$. Although there are some outliers, there should be no important statistical differences
 213 in our Sn/Lg analysis when selecting either of these two Sn/Lg calculation methods. Accordingly, RMS
 214 amplitudes are used throughout this paper.

215



216

217

218 **Fig. S4. Difference between Sn/Lg RMS ratios and Sn/Lg Peak ratios for all events with acceptable SNR .**

219 Horizontal value is the average $\ln(Sn/Lg)$ which is the average between the two types of Sn/Lg ratios.

220

221

222

223

224

225

226

227

228

229

230

231

232 **S5. Geometric spreading detrend**

233

234 The recorded amplitude is influenced by multiple effects (Hasegawa, 1985; Wang and Klemperer, 2021):

235

$$A(f, R) = S(f)G(R, f)\psi(R, f)I(f)P(f) \quad (S5.1)$$

236

237 where A is the recorded amplitude, S is the source amplitude, G is the geometric spreading factor, ψ is the
 238 intrinsic attenuation, I is the instrument response, P is the site response, and R is the epicentral distance. For a
 239 single station, I and P can be neglected. ψ is discussed in the main paper (Section 5-Discussion). We use a
 240 theoretically derived G to detrend our data. Even though this is a second order correction to the Sn/Lg ratios, it
 241 is helpful in comparing the results from two regions with different receiver distances, albeit unnecessary for
 242 Sn/Lg analysis in a small region.

243

244 We approximate $G(R, f)$ for Sn and Lg (Fan and Lay, 2003; Wang and Klemperer, 2021; Yang, 2002; Fig. S5).
 245 We assume $\log_{10}(G_{Sn})$ is flat out to 800 km distance then increases at 0.0006/km. we assume $\log_{10}(G_{Lg})$ to
 246 decrease at 0.00025/km. Using a reference distance of 500 km, we detrend our data by multiplying the
 247 amplitudes, A_{Sn} and A_{Lg} , with the coefficients:

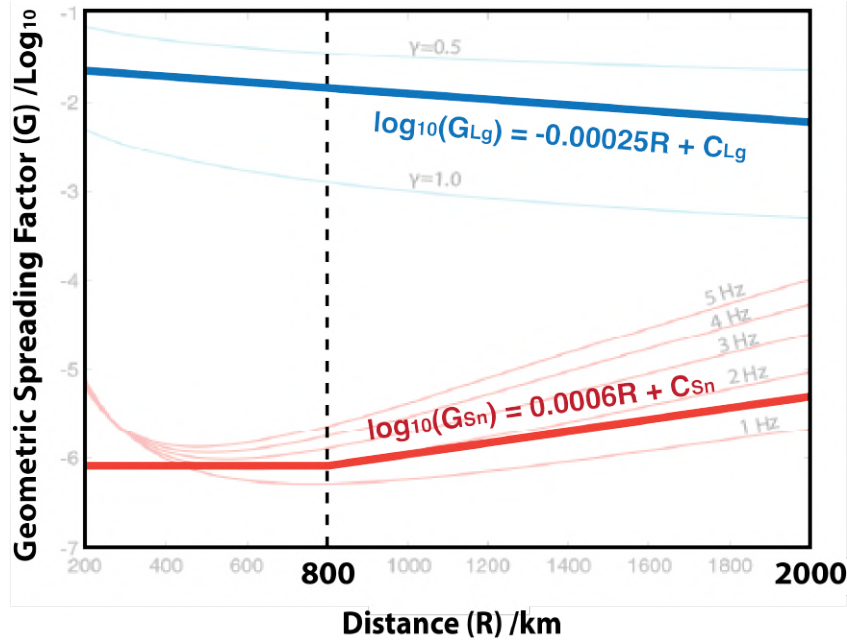
248

$$K_{Sn} = -10^{[(0, R - 800 \text{ km})_{max} * 0.0006/\text{km}]} \quad (S5.2a)$$

$$K_{Lg} = 10^{[(R - 500 \text{ km}) * 0.00025/\text{km}]} \quad (S5.2b)$$

249

250



251

252

253 **Fig. S5. Geometric spreading curves $G(R, f)$ for Sn (red) and Lg (blue) from Wang and Klemperer (2021) for**
 254 **different frequency & γ (Lg spreading exponent). Thick lines represent the simplified function used for detrending in**
 255 **this research. C_{Sn} and C_{Lg} are arbitrary constants.**

256

257

258

259

260

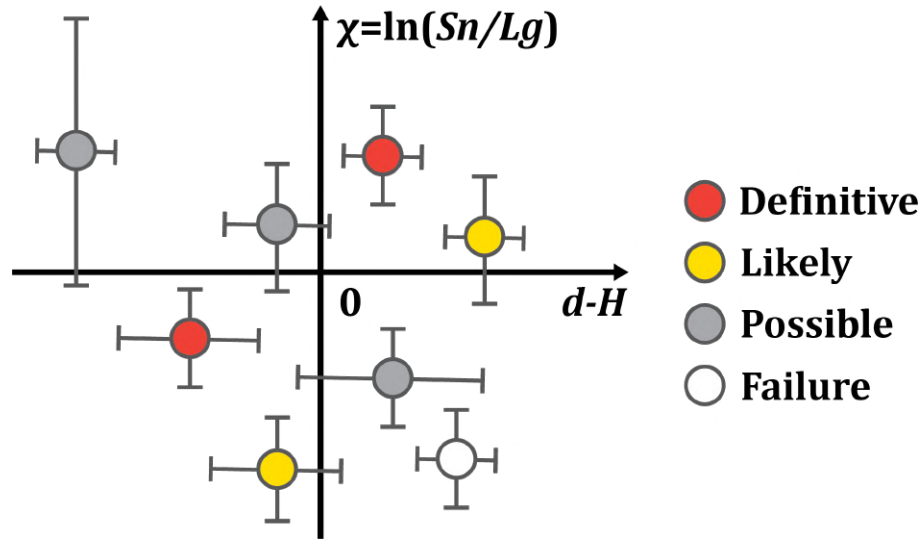
261

262

263 **S6. Earthquake classifications**

264
265
266
267
268
269
270
271
272
273

We classify the earthquakes we studied into the following categories: “definitive” represents the events that the S_n/L_g and depth agree even considering the worst situation that the uncertainty allows; “likely” represents the other events for which S_n/L_g and depth agree without considering uncertainties; and “possible” represents remaining events for which S_n/L_g and depth agrees within uncertainty (Fig. S6, Table 6-1). The small number of events for which the S_n/L_g ratio predicts an incorrect location with respect to Moho, even after allowing for uncertainty, are considered as failures of our method. Note that depth errors are as specified by the source catalogs and the Moho determination is assigned zero error; if these errors are too small some ‘definitive’ events will be downgraded to ‘likely’, and some ‘failures’ could become ‘possible’ successes.



274
275
276
277
278
279
280
281
282
283
284
285
286
287
288
289
290
291
292
293
294
295
296
297
298
299
300

Fig. S6. Earthquake classification criteria.

Using only the ‘better-located’ earthquakes, we have a >70% success rate and <10% failure rate (Table S6-1), and indeed if we ignore SE Tibet where the Moho depth is less-well known our success rate increases to 90% and the failure rate drops to 5%. When we include the PDE-only events (Table S6-2), these percentages do not change drastically, but we see a very large proportional increase in the number of above-Moho events (for WT we show 34 below-Moho and 5 above-Moho ‘better-located’ events, but 38 below- and 91 above-Moho PDE-only events. We doubt these changed proportions represents bias in the GCMT and ISC-GEM catalogs even though these are only complete for $m > 5$ earthquakes (Ammon et al., 2021; Storchak et al., 2013), because GCMT or ISC-GEM only contribute ~15% of ‘better-located’ events in WT and ~40% for our entire Tibet catalog. A modest effect could be the greater attention paid to deeper earthquakes, so increasing the probability that below-Moho events are over-represented in the ‘better-located’ category. However, we expect that the increased number of above-Moho events include a very substantial fraction of shallow seismicity mis-located in the PDE catalog: Fig. S3-2a suggests that >60% of the PDE-only events with catalog depths 30–60 km may in fact be upper-crustal earthquakes <30 km, corresponding to ~200 excess events on our cross-sections at 30–60 km. Additionally, as noted in Supplementary Material S3, we statistically expect that 10–20 events that are only in the PDE catalog are grossly mislocated, e.g., with true sub-Moho depths but located in the upper crust, or vice versa, so if correctly determined with respect to Moho by our S_n/L_g method would be recorded as failures of our method. These events could represent a substantial fraction of the ~50 total failures recorded in Table S6-2 compared to the 15 failures in Table S6-1.

301
302
303
304

Table S6-1. Classification of ‘better-located’ earthquakes (stars in Figs. 4–7) based on the catalog depths, RF Moho depths, Sn/Lg ratios, and their uncertainties.

Region	Definitive		Likely & Definitive		Possible		Failure	Success Rate	Failure Rate
	Sub Moho	Above Moho	Sub Moho	Above Moho	Sub Moho	Above Moho			
	$\chi > \sigma_\chi$ $d - H > \sigma_d$	$\chi < -\sigma_\chi$ $d - H < -\sigma_d$	$\chi > 0$ $d - H > 0$	$\chi < 0$ $d - H < 0$	$\chi > 0$ $-\sigma_d < d - H < 0$ Or $-\sigma_\chi < \chi < 0$ $d - H > \sigma_d$	$\chi < 0$ $0 < d - H < \sigma_d$ Or $0 < \chi < \sigma_\chi$ $d - H < -\sigma_d$			
WT	21	4	34	5	1	0	2	93%	5%
ST	13	6	20	13	2	0	2	89%	5%
SET	8	11	21	28	9	13	9	61%	11%
SWT (KBL)	0	1	0	1	0	0	0	-	-
SWT (LSA)	0	2	0	2	0	1	2	-	-
QT	0	1	0	1	0	0	0	-	-

305
306
307
308
309
310

* $\chi = \ln(Sn/Lg)$

Table S6-2. As Table S6-1, but for all earthquakes, including PDE-only events.

Region	Definitive		Likely & Definitive		Possible		Failure	Success Rate	Failure Rate
	Sub Moho	Above Moho	Sub Moho	Above Moho	Sub Moho	Above Moho			
	$\chi > \sigma_\chi$ $d - H > \sigma_d$	$\chi < -\sigma_\chi$ $d - H < -\sigma_d$	$\chi > 0$ $d - H > 0$	$\chi < 0$ $d - H < 0$	$\chi > 0$ $-\sigma_d < d - H < 0$ Or $-\sigma_\chi < \chi < 0$ $d - H > \sigma_d$	$\chi < 0$ $0 < d - H < \sigma_d$ Or $0 < \chi < \sigma_\chi$ $d - H < -\sigma_d$			
WT	50	71	72	96	7	12	9	86%	5%
ST	25	24	40	50	7	4	12	80%	11%
SET	26	16	53	42	19	33	25	53%	15%
SWT (KBL)	0	21	0	28	0	1	1	93%	3%
SWT (LSA)	0	14	4	29	1	9	4	70%	9%
QT	0	27	0	44	0	11	1	79%	2%

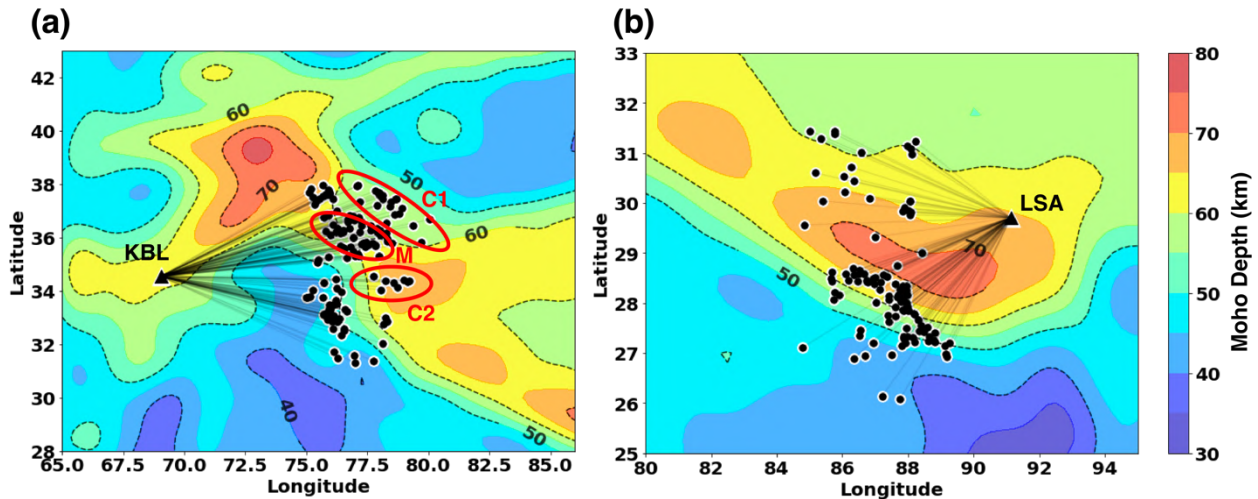
311
312
313
314
315
316
317
318
319
320

* $\chi = \ln(Sn/Lg)$

321 **S7. S_n and L_g Blockage or Leakage**

322
323
324
325
326
327
328
329
330
331
332
333
334
335
336
337
338
339
340
341

The normal-mode synthetics for S_n/L_g (Fig. 3; Wang and Klemperer, 2021) are calculated for 1-D earth models, but it is well-known that structural boundaries (e.g., Moho ramps, Fig. 2B) can modify S_n & L_g amplitudes (Kennett, 1986). The obvious binary classification and clear separation of apparently above-Moho from below-Moho earthquakes in WT (Fig. 4) suggests S_n or L_g blockage can only be a secondary-order effect. Nonetheless, we plot ray paths from the WT earthquakes to KBL on a recent Moho map (Fig. S6) inferred from gravity measurements (Zhao et al., 2020) (the RF Moho map used in Fig. 4 (Xia et al., 2022) does not extend west to KBL;). Raypaths from many earthquakes in WT1 (north half) are crudely parallel to the Moho contours, so should be little affected by S_n or L_g blockage. The northeasternmost band of earthquakes (C1 in Fig. S7a) above a 55 km Moho and beneath WKT (Fig. 4) are all above Moho based both on reported depths and their low S_n/L_g , consistent with crustal paths and hence no L_g blockage. Similarly the earthquakes labelled M (Fig. S7a) beneath the surface traces of the JRS & ATF (Fig. 4) are likely all south of the ATF at depth (Wang and Klemperer, 2021) so their below-Moho assignment based on hypocentral depth and high S_n/L_g is consistent with no S_n blockage as energy travels from thicker crust to the SE. The earthquakes C2 (Fig. S7) have ray paths from thick to thin crust, so would be expected to show L_g blockage (Fig. 2B, left) but nonetheless have low S_n/L_g consistent with their nominally crustal hypocenters. Perhaps any L_g blockage in transiting from thick Tibetan crust to thin Indian crust is balanced by S_n blockage when transiting from thin Indian crust to thick Hindu Kush crust. In summary however, we have no clear examples of S_n or L_g blockage being an important effect between WT and KBL.



342
343
344
345
346
347
348
349
350
351
352
353
354
355
356
357
358
359

Fig. S7. Ray paths superimposed on the Moho map of Zhao et al. (2020). (a) WT earthquakes recorded at KBL. (b) ST earthquakes recorded at LSA.

Earthquakes from south Tibet recorded at LSA (Figs. 5, S7b) have a less-clear binary classification than the WT earthquakes recorded at KBL, but we have not found systematic changes in S_n/L_g ratios that we can associate with S_n or L_g blockage. The large discrepancy between receiver-function Moho (Xia et al., 2022) and gravity Moho (Zhao et al., 2020) (Fig. 5c) may as noted in the main text be indicative of partial eclogitization that can modify S_n/L_g ratios (Fig. 3b).

360 **S8. Filter applied to the Moho map**

361

362 We apply an elliptical 100×200 km Gaussian filter to the raw Moho data map of Xia et al. (2022) to get a
363 representative Moho profile in our cross-sectional plots. This filter has its short axis across tectonic strike,
364 along the profile. Standard deviations of the Gaussian filter are half of the respective axis lengths (50 km along
365 the profile, 100 k across the profile).

366

367

368

369 **S9. Comparison between LSA and KBL in west Tibet**

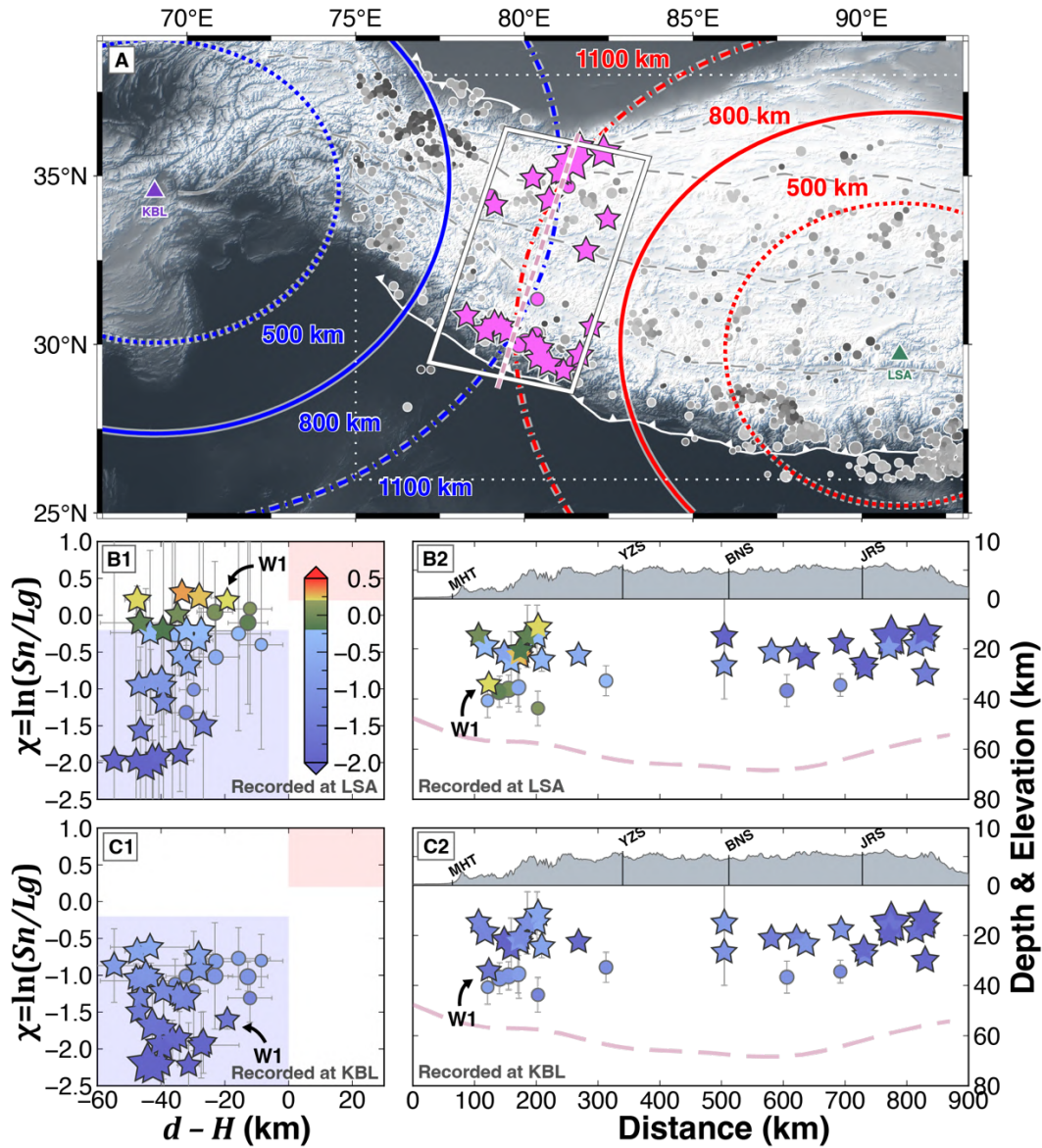
370

371 We select the region in which earthquakes are roughly equidistant (~ 900 - 1300 km) from Kabul and Lhasa, for
372 comparison of S_n/L_g as recorded at each station (Fig. S9). 38 earthquakes below 30 km (magenta stars and
373 circles in Fig. S9), including 8 PDE events and 30 events from GCMT and ISC, passed our SNR criteria at both
374 stations. All these earthquakes are located in the crust.

375

376 Earthquakes in the north part of the selected region (Qiangtang) have similar low S_n/L_g ratios at both LSA and
377 KBL's records. However, earthquakes located south of the YZS on average have higher S_n/L_g ratios at LSA,
378 including several events with "intermediate" or weak "mantle" S_n/L_g , including W1 (Fig. S9-B1). These
379 differences are likely the result of lower L_g and higher crustal attenuation for Tibetan ray paths to LSA than for
380 Indian ray paths to KBL (Fig. S7) (Taylor et al., 2003), as is also suggested by the noisier records (having larger
381 S_n/L_g uncertainties) at Lhasa than at Kabul. Analogous effects have been explicitly shown for single Tibetan
382 earthquakes recorded on 2D arrays that cross regions of different attenuation (Wang & Klemperer, 2021, their
383 Fig. 7). L_g blockage due to Moho topography is probably not the cause (Supplementary Material S7): these
384 eight earthquakes' ray paths to Lhasa travel through crust that is never thinner than at the hypocenter, so should
385 not experience any L_g blockage (Kennett, 1986).

386



387
 388
 389 **Fig. S9. (A)** Earthquakes recorded with sufficient *SNR* at both KBL and LSA (magenta circles and stars). Red
 390 and blue circles represent the equidistance circles of IC.LSA and IU.KBL respectively (dotted: 500 km; solid:
 391 800 km; dash dotted: 1100 km). White frame marks the region in which earthquakes have nearly the same distance
 392 to the two stations. Gray smaller dots are the other earthquakes in our catalog. Dashed pink line is the line of cross-
 393 section in B2 & C2. **(B1 & C1)** *Sn/Lg* vs *d - H* plots for the selected earthquakes from IC.LSA and IU.KBL
 394 respectively. Legends as in Fig. 5B, but *Sn/Lg* color bar is modified to range from -1.0 to 0.5 . **(B2 & C2):** Cross-
 395 sectional view of the *Sn/Lg* ratios for the selected earthquakes from IC.LSA and IU.KBL respectively. Legends
 396 as in Fig. 5C.
 397
 398
 399
 400
 401
 402
 403
 404

405 **S10. S_n/L_g results from the Qiangtang**

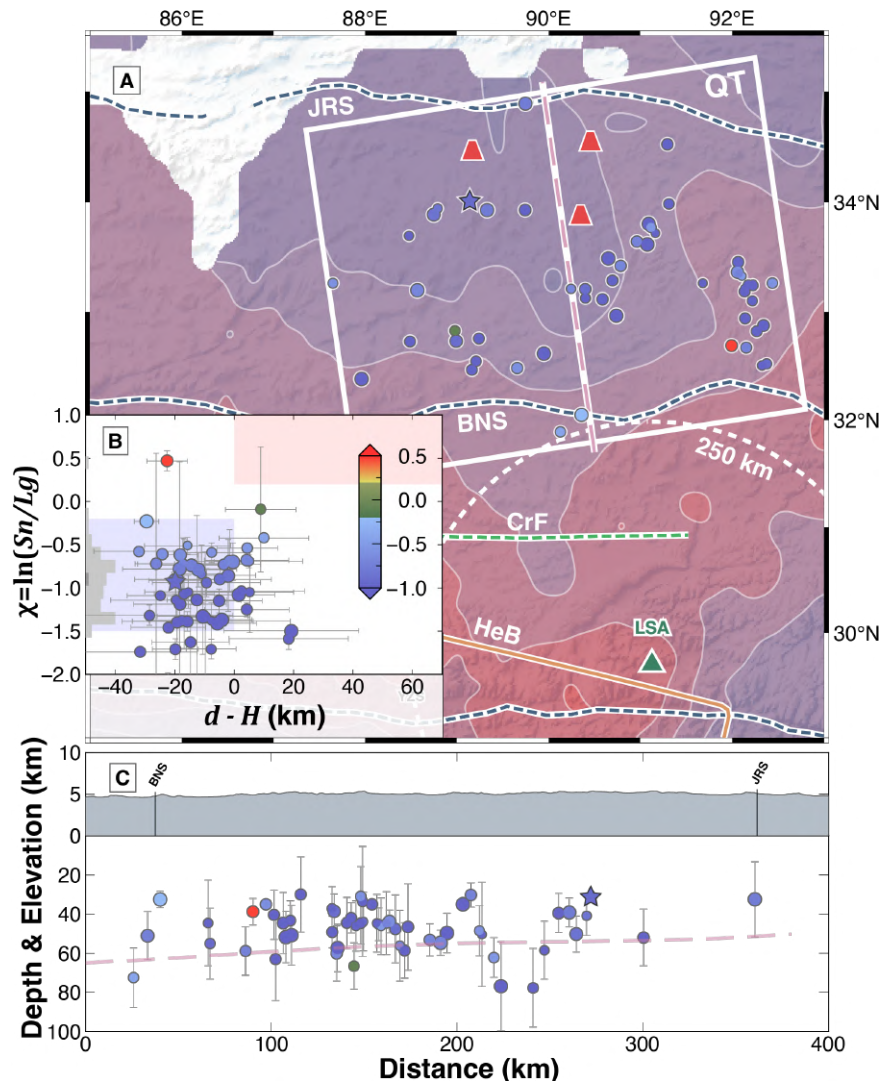
406

407 We obtain the S_n/L_g ratios of 56 earthquakes in the eastern Qiangtang (QT), a region identified with high S_n
 408 attenuation and likely high mantle temperature (McNamara et al., 1995b). Most earthquakes in this region are
 409 nominally crustal, and all but one have low S_n/L_g ratios. All 10 earthquakes nominally below the Moho are
 410 within depth uncertainty of the Moho, and nine have low S_n/L_g and one has intermediate S_n/L_g (with large
 411 uncertainty). Considering the large depth uncertainties for these earthquakes and the lack of apparent depth-
 412 dependent S_n/L_g , we conclude there is no evidence for mantle seismicity in the Qiangtang. The average S_n/L_g
 413 ratios in QT are lower than those in ST, SET, and SWT, consistent with strong source-side S_n attenuation in the
 414 Qiangtang.

415

416 The apparent existence of ~50 earthquakes nominally in the lower-crust of the hottest part of Tibet is remarkable
 417 given that the temperature likely exceeds 700°C at 25-km depth (Wang et al., 2016). Comparison of PDE depths
 418 and ‘better-located’ depths (Fig. S3-2) suggests that one-third of these 50 earthquakes likely have true
 419 hypocenters at >30 km depth.

420



421

422

423 **Fig. S10. (A) S_n/L_g ratio spatial distribution in Qiangtang (QT).** Legends as in Fig. S4 (A). Red trapezoids:
 424 quaternary volcanoes (Wang et al., 2016). (b) $\ln(S_n/L_g)$ vs $d - H$ plots for QT. Legends the same with Fig. 5 (b).
 425 (c) Cross-sectional view of the S_n/L_g ratios along the profile direction in (A). Legends the same with Fig. 5C.

426
427
428
429
430
431
432
433
434
435
436
437
438
439
440
441
442
443
444
445
446
447
448
449
450
451
452
453
454
455
456
457
458
459
460
461
462
463
464
465
466
467
468
469
470
471
472
473
474
475
476
477
478

References:

Ammon, C.J., Velasco, A.A., Lay, T., Wallace, T.C., 2021. Chapter 19 - Imaging seismic-sources, in: Ammon, C.J., Velasco, A.A., Lay, T., Wallace, T.C. (Eds.), *Foundations of Modern Global Seismology (Second Edition)*. Academic Press, pp. 515–535. <https://doi.org/10.1016/B978-0-12-815679-7.00027-6>

Fan, G.-W., Lay, T., 2003. Strong Lg wave attenuation in the Northern and Eastern Tibetan Plateau measured by a two-station/two-event stacking method. *Geophys. Res. Lett.* 30. <https://doi.org/10.1029/2002GL016211>

Jiang M., Zhou S., Tong X., Liang X., Chen Y., 2009. Accurate depth determination of deep earthquake in southern Tibet and its geodynamic implication. *Chin. J. Geophys.* 52, 2237–2244. <https://doi.org/10.3969/j.issn.0001-5733.2009.09.007>

Kennett, B.L.N., 1986. Lg waves and structural boundaries. *Bull. Seismol. Soc. Am.* 76, 1133–1141. <https://doi.org/10.1785/BSSA0760041133>

McNamara, D.E., Owens, T.J., Walter, W.R., 1995. Observations of regional phase propagation across the Tibetan Plateau. *J. Geophys. Res. Solid Earth* 100, 22215–22229. <https://doi.org/10.1029/95JB01863>

Michailos, K., Carpenter, N.S., Hetényi, G., 2021. Spatio-Temporal Evolution of Intermediate-Depth Seismicity Beneath the Himalayas: Implications for Metamorphism and Tectonics. *Front. Earth Sci.* 9.

Monsalve, G., Sheehan, A., Schulte-Pelkum, V., Rajaure, S., Pandey, M.R., Wu, F., 2006. Seismicity and one-dimensional velocity structure of the Himalayan collision zone: Earthquakes in the crust and upper mantle. *J. Geophys. Res. Solid Earth* 111. <https://doi.org/10.1029/2005JB004062>

Mousavi, S.M., Cramer, C.H., Langston, C.A., 2014. Average QLg, QSn, and observation of Lg blockage in the Continental Margin of Nova Scotia. *J. Geophys. Res. Solid Earth* 119, 7722–7744. <https://doi.org/10.1002/2014JB011237>

Storchak, D.A., Di Giacomo, D., Bondar, I., Engdahl, E.R., Harris, J., Lee, W.H.K., Villasenor, A., Bormann, P., 2013. Public Release of the ISC-GEM Global Instrumental Earthquake Catalogue (1900-2009). *Seismol. Res. Lett.* 84, 810–815. <https://doi.org/10.1785/0220130034>

Taylor, S.R., Yang, X., Phillips, W.S., 2003. Bayesian Lg Attenuation Tomography Applied to Eastern Asia. *Bull. Seismol. Soc. Am.* 93, 795–803. <https://doi.org/10.1785/0120020010>

Wang, Q., Hawkesworth, C.J., Wyman, D., Chung, S.-L., Wu, F.-Y., Li, X.-H., Li, Z.-X., Gou, G.-N., Zhang, X.-Z., Tang, G.-J., Dan, W., Ma, L., Dong, Y.-H., 2016. Pliocene-Quaternary crustal melting in central and northern Tibet and insights into crustal flow. *Nat. Commun.* 7, 11888. <https://doi.org/10.1038/ncomms11888>

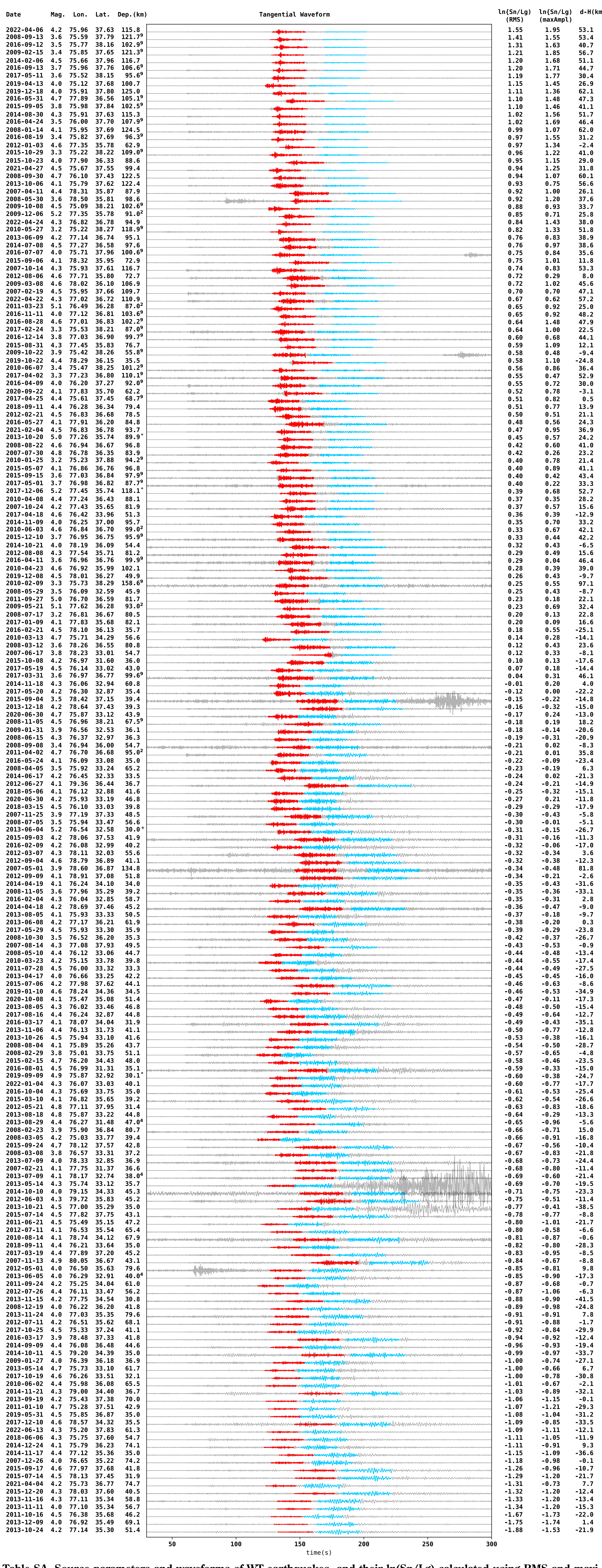
Wang, S., Klemperer, S.L., 2021. Love-wave normal modes discriminate between upper-mantle and crustal earthquakes: Simulation and demonstration in Tibet. *Earth Planet. Sci. Lett.* 571, 117089. <https://doi.org/10.1016/j.epsl.2021.117089>

Xia, B., Artemieva, I., Thybo, H., Klemperer, S., 2022. Regional variability in the thermal structure of Tibetan Lithosphere (No. EGU22-7161). Presented at the EGU22, Copernicus Meetings. <https://doi.org/10.5194/egusphere-egu22-7161>

Yang, X., 2002. A Numerical Investigation of Lg Geometrical Spreading. *Bull. Seismol. Soc. Am.* 92, 3067–3079. <https://doi.org/10.1785/0120020046>

Zhao, G., Liu, J., Chen, B., Kaban, Mikhail.K., Zheng, X., 2020. Moho Beneath Tibet Based on a Joint Analysis of Gravity and Seismic Data. *Geochem. Geophys. Geosystems* 21, e2019GC008849. <https://doi.org/10.1029/2019GC008849>

Zhao, L.-S., Helmberger, D.V., Harkrider, D.G., 1991. Shear-velocity structure of the crust and upper mantle beneath the Tibetan Plateau and southeastern China. *Geophys. J. Int.* 105, 713–730. <https://doi.org/10.1111/j.1365-246X.1991.tb00807.x>



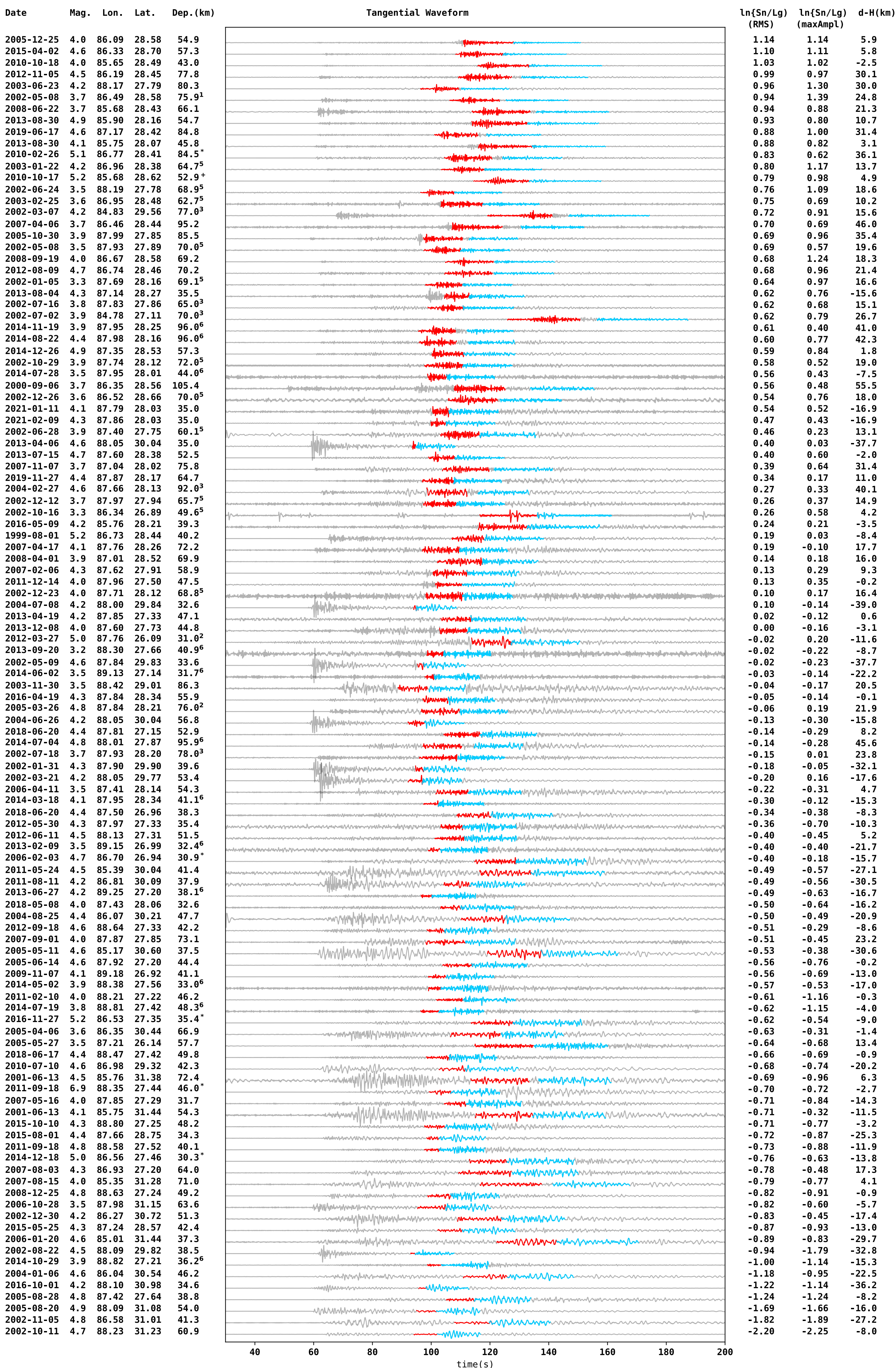


Table SB. Source parameters and waveforms of ST earthquakes, and their $\ln(Sn/Lg)$ calculated using RMS and maximum amplitude ratios. Waveforms aligned by P arrival (set to be 60 s here).

Depths listed are from the PDE catalog except where marked with a superscript: 1: Alvizuri and Hetényi, (2019); 2: Craig et al., (2012); 3: Baur, (2007); 4: Parija et al., (2018); 5: Michailos et al., (2021); 6: Diehl et al., (2017); 7: Monsalve et al., (2006); 8: Jiang et al., (2009); 9: Bloch et al., (2021); *: GCMT; +: ISC-GEM.

